Development and Synthesis of Mononuclear Superoxide Dismutase Mimics and Magnetic Resonance Imaging Contrast Agents

by

Tessa Hutchinson

A dissertation submitted to the Graduate Faculty of
Auburn University
in partial fulfillment of the
requirements for the Degree of
Master of Science

Auburn, Alabama
[May 1, 2021]

Keywords: [Contrast agent, T_1-relaxtion, Reactive Oxygen Species, Magnetic Resonance Imaging, Superoxide Dismutase]

Approved by

Christian R. Goldsmith, Chair, Professor of Chemistry and Biochemistry
Evert Duin, Professor of Chemistry and Biochemistry
Byron H. Farnum, Assistant Professor of Chemistry and Biochemistry

Abstract

Over the past few years the Goldsmith group has reported mononuclear superoxide dismutase mimics and Mn(II) complexes with redox-active quinols that display rapid *T1*-weighted responses to H_2O_2. This dissertation will focus upon the development and synthesis of two mononuclear potential SOD mimics containing Fe(II) and Co(II) respectively; as well as, two manganese based MRI contrast agents. MRI is chosen as a spectroscopic technique due to its ability to non-invasively monitor biochemical processes in organs and whole-body subjects. The SOD mimics and contrast agents can be used to study a wide range of other health conditions that have been correlated to oxidative stress, heightening the extrinsic value of this work.

Firstly discussed is the SOD activity of the new Fe(II) and Co(II) complexes. Prior Mn(II) complexes reported by the Goldsmith group were found to catalytically degrade superoxide. The greater stability of the developed compounds is anticipated to lengthen the lifetime of the catalyst in biological environments, yielding a much more effective anti-oxidant. Secondly discussed is the *T1*-related relaxivity (*r1*) of two manganese containing MRI contrast agents. H_6qc1 showed a very strong binding affinity for Mn(II), but no response *r1* response. It is thought that even with a strong binding affinity, upon oxidation the ligand and metal are both oxidized resulting in no response to H_2O_2. H_3qpc, has been designed with ligands H_4qp2 and H_6qc1 in mind, and has shown no metal oxidation with promising responses to H_2O_2.

Acknowledgments

I would like to thank Dr. Christian Goldsmith for helping me with my research endeavors and helping me gain so much experience and knowledge. I would like to thank my husband for all his kind words, encouragement, and help. I would also like to thank my parents and family for their unyielding support for me and my dreams. I would also like to thank my fellow graduate students in helping each other make it through, as well as all my lab mates and undergraduate research assistants. It truly does take a village and I am so honored to have been a part of this one.

Table of Contents

List of Tables

List of Figures

List of Abbreviations

·OH	Peroxide Radical
BOLD	Blood Oxygenated Level Dependent
CEST	Chemical Exchange Saturation Transfer
Co	Cobalt
Cu	Copper
DCM	dichloromethane (CH_2Cl_2)
EDTA	Ethylenediamine tetraacedic acid
EPR	Electron Paramagnetic Resonance
Ether	Diethyl ether
EtOAc	ethyl acetate
EtOH	ethanol
Fe	Iron
H_2O_2	Hydrogen Peroxide
H_6qc1	*N,N'*-bis(2,5-dihydroxybenzyl)ethanediamine-*N,N'*-diacetic acid
HBED	*N,N'*-bis(2-hydroxybenzyl)ethylenediamine-*N,N'*-diacetic acid
HCl	Hydrochloric acid
Hptp1	N-(2-Hydroxy-5-methyl-benzyl)-N,N',N'-tris(2-pyridinylmethyl)-1,2-ethanediamine
IR	Infrared Spectrometry
KBr	Potassium Bromide
KCl	Potassium Chloride
KOH	Potassium Hydroxide
MCD	Magnetic Circular Dichroism

MeCN	Acetonitrile
MeOH	methanol
Mn	Manganese
MnSODm	Manganese SOD mimics
MRI	Magnetic Resonance Imaging
MS	Mass Spectrometry
NEt_3	Triethyl amine
NMR	Nuclear Magnetic Resonance
O_2^-	Superoxide anion
Otf_3	Triflate
PET	Positron Emission Tomography
q	Aquation number
*r*1	Rate of relaxation, 1/*T1*
ROS	Reactive Oxygen Species
SOD	Superoxide Dismutase
TBAF	Tetra-*N*-butylammonium fluoride
THF	Tetrahydrofuran
TIS	Triisopropylsilane
UV-VIS	Ultraviolet visible spectrometry
Zn	Zinc

Chapter 1

Redox active magnetic resonance imaging contrast agents

1.1 Biological processes and disorders

Reactive oxygen species (ROS) include hydroxyl radicals (·OH), superoxide anions (O_2^-), and hydrogen peroxide (H_2O_2). ROSs are produced within the mitochondria and various other electron transfer regions within cells.[1-3] ROS levels are regulated by antioxidants such as superoxidase dismutase (SOD). When ROSs rise to levels that cannot be managed by the body's antioxidants, this creates oxidative stress, which has been linked to cancer[4-7], heart disease[8-14], inflammatory disorders[15-17], neurological disorders[18-22], and aging.[23,24] Given these connections, there is great interest in developing ways to monitor and control ROS concentrations.

1.2 Current ROS detection

There are many methods for ROS detection from the most basic of measurements including blood oxygenated level dependent (BOLD MRI)[25,26], ^{19}F MRI[27,28] , fluorescent probes[25,29,30] , chemical exchange saturation transfer (CEST)[31] , and positron emission tomography (PET)[32]. Numerous SOD mimics and imaging agents have been tested and used for ROS regulation and detection. However, most imaging agents are impractical due to 1) high incidences of false positives, 2) instability in biological conditions, 3) toxicity, 4) the necessity for a co-analyte, 5) a turn-off response to one or more ROS, and/or 6) incompatibility with non-invasive imaging techniques. To address this need, I propose to develop novel magnetic resonance imaging (MRI) contrast agents that can detect the ROS H_2O_2 through an increase in *T1*-weighted relaxivity.

1.3 Instrumentation: Magnetic Resonance Imaging

MRI is a non-invasive spectroscopic technique commonly used to visualize internal tissues and organs. MRI instruments create a magnetic field that renders the +1/2 and -1/2 spin-

states of ^{1}H nuclei non-degenerate. Radiofrequency pulses promote the ^{1}H protons to the higher spin-state, out of alignment with the magnetic field. After the pulse, the protons relax back into alignment with the magnetic field. MRI sensors detect the energy released by the return to the magnetization equilibrium and converts the data into an image (Figure 1.1).

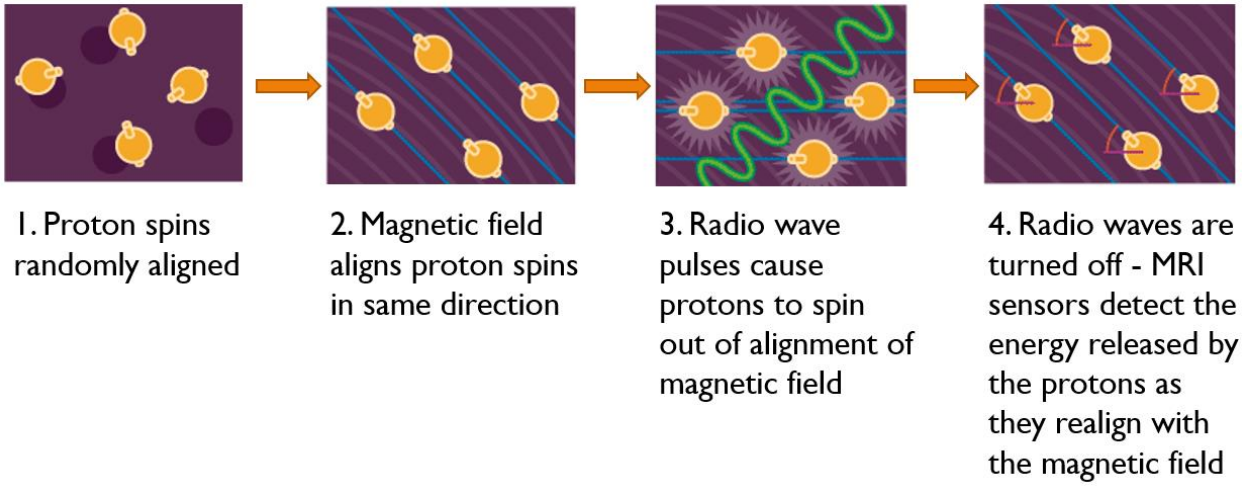

Figure 1.1: Illustration of how MRI operates.[33]

The signal depends both on the concentration of protons, which normally scales with the water content, and the rate of relaxation. The rate of relaxation, 1/*T1*, is denoted *r1*. Increasing *r1* leads to enhanced MRI contrast, and *T1*-weighted contrast agents are consequently known as positive contrast agents.[34,35] These are the most popularly used contrast agents and usually contain highly paramagnetic metal ions, such as Gd^{3+} and Mn^{2+}.

1.4 Contrast agent design

Paramagnetic metal ions increase *r1* by introducing new relaxation pathways for bound water molecules. An appropriate rate of water molecule exchange is needed to observe a decrease in *T1*. The relaxivity rate not only depends upon the metal ion used, but also the ligand. The ligand impacts the molecular tumbling, which is simply the rotation of the molecule itself.[27] Smaller ligands lead to faster rates of molecular tumbling and slower water molecule exchange,

producing lower contrast images. The aquation number (q), which is the number of water molecules directly coordinated to the metal ion, is another key factor in determining *r1*. Higher values of q lead to higher *r1*, and the ligand of a MRI contrast agent can modulate q (and thereby *r1*) by limiting the number of available coordination sites for water (Figure 1.2).[35] Although less highly coordinating ligands can allow high q values, their complexes with the labile metal ions used for MRI are insufficiently stable for use in water.

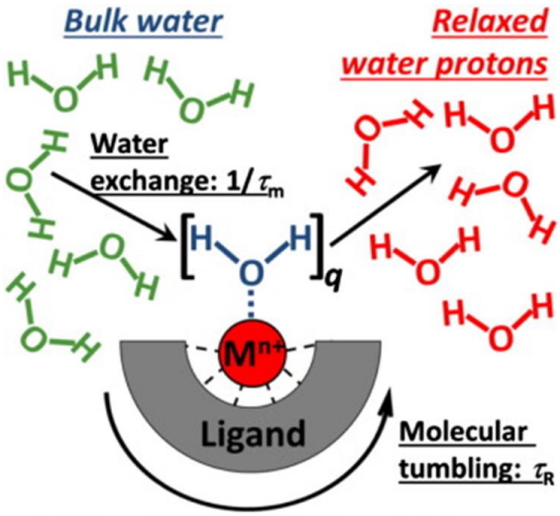

Figure 1.2: Illustration of factors involved in relaxivity.[27]

Contrast agents that are being researched today include mononuclear coordination complexes and nanoparticles.[36-45] The most popular mononuclear contrast agents, like Magnevist, contain Gd^{3+}, which has a 7/2 spin. The large spin allows for higher relaxation rates and substantially enhanced contrast. However, gadolinium agents require strongly coordinating ligands to prevent the release of free Gd^{3+}. Since this is a non-native metal ion, biology has no mechanisms in place to regulate Gd^{3+}.[42,43] In previous studies, gadolinium has been found to be a "bone-seeking" ion and can replace calcium deposits within bone and brain tissues.[42,43] With respect to ROS detection, the redox-inactivity of Gd^{3+} would require a ligand capable of reacting with one or more ROS entirely by itself. Nanoparticles have shown to be too big to cross cell membranes, limiting their applicability.[38] Consequently, these classes will not be discussed further in this proposal.

Studies have shown that Mn^{2+} ions coordinated to various forms of carboxylates or carboxylate containing ligands can enable high MRI contrast that matches those of clinically

used gadolinium agents. Mn^{2+} is highly paramagnetic, with a spin-state of 5/2 allowing for a high *r1*. Further, Mn^{2+} is native to biological systems, and cells have mechanisms in place to properly manage its levels. Manganese can be excreted through the liver and gall bladder quickly, not allowing for ion replacement or collection in tissues.[45] The tolerable upper intake level of manganese per day is 11 mg for adults which is higher than those for other redox-active metals; nickel, for example, has an upper intake level of 1 mg/day.[46]

1.5 Previous redox-responsive MRI Contrast agents

As stated earlier, there are many redox-responsive MRI contrast agents being explored including nanoparticles and lanthanide containing MRI contrast agents. Further attention to MRI contrast agents will focus on first row transition metals, particularly manganese as it pertains most to this research. The redox activity of previously characterized manganese complexes used for either MRI or SOD mimicry has mainly been limited to the oxidation state of the metal, specifically the +2 and +3 oxidation states. Peter Caravan's research group has done a series of studies on Mn-containing MRI redox-active contrast agents that display increased *r1* upon reduction and decreased *r1* upon oxidation.[28,50,51] Oxidation to Mn^{3+} produces an ion with S = 2; the lesser paramagnetism necessarily lowers *r1*.

1.6 Superoxide (SOD) Mimics

Manganese complexes are attractive not only as MRI contrast agents but also as SOD mimics. Manganese SOD mimics, MnSODm, have been studied for years.[47-49] The basic chemical process of SOD activity can be seen in Scheme 1.1. These SOD mimics share many design requirements with contrast agents to improve efficiency including aqueous stability and ligand structure including exchangeable sites for exogenous monodentate ligands. They also

share the same dependency of redox active metal centers. Policar and coworkers have researched a series of MnSODm in which the oxidation state of the manganese toggles between +2 and +3 during the catalysis of superoxide degradation.[52,53] Comparative research has also been performed on a series of SOD mimics containing Mn, Fe, Cu, and Zn by collaborators Ivana Ivanović-Burmazović and coworkers.[47-49,53,55,57] Few SOD mimic studies have been conducted using Co alone, and usually introduce this metal into active sites of proteins paired with Zn. For this reason, Co will be used along with Fe in these SOD mimic experiments, and Co will be a control. This research proposes to develop manganese complexes capable of an enhanced MRI response to ROS and iron SOD mimicry that rely on changes to the oxidation state of the ligand, rather than the metal.

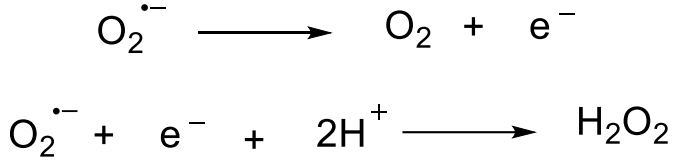

Scheme 1.1: Basic chemical equation of superoxide dismutase

1.7 Goldsmith group contrast agents

Prior work in our lab developed three redox-active ligands: Hptp1, H_2qp1, and H_4qp2 (Scheme 1.2).

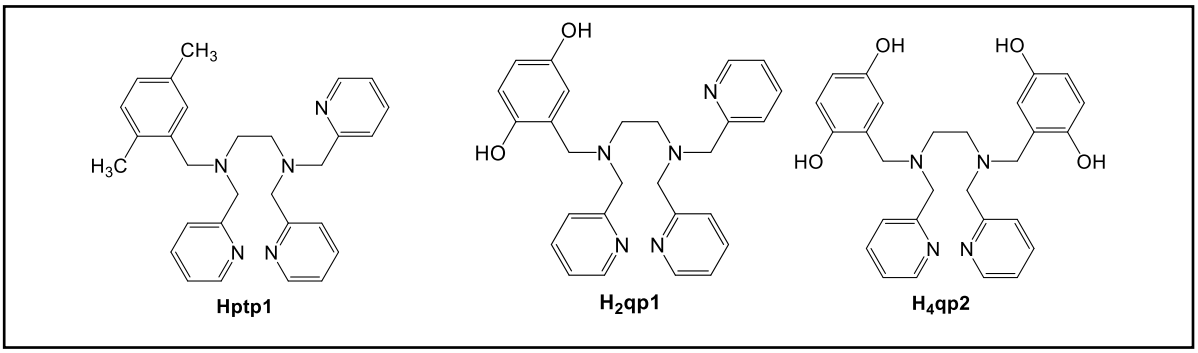

Scheme 1.2: Redox-active ligands: Hptp1, H_2qtp1, and H_4qtp2.[54-56]

The Mn^{2+} complex with the Hptp1 ligand was found to have a heptacoordinate distorted pentagonal bipyramidal geometry as a mononuclear crystal. It is measured relaxivity of the

mononuclear complex was 4.39 $mM^{-1}s^{-1}$ in 50 mM HEPES buffered water with pH of 7.00. However, upon exposure to H_2O_2 caused the mononuclear manganese complex to undergo oxidative coupling to form a binuclear manganese complex with a lower measure relaxivity of 3.59 $mM^{-1}s^{-1}$ in same solution as previous measurement.[54] The MnHptp1 complex was also recently characterized as a SOD mimic; the redox activity of the ligand prolongs the catalysis by diverting ROS side-products into an innocuous coupling reaction.[55] This coupling reaction also occurs upon addition of H_2O_2 to a solution of the mononuclear Mn-Hptp1 complex. The metal is transiently oxidized, as evidenced by the solution, and MS analysis and crystallization show a dinuclear Mn^{2+} product (Figure 1.3).[55]

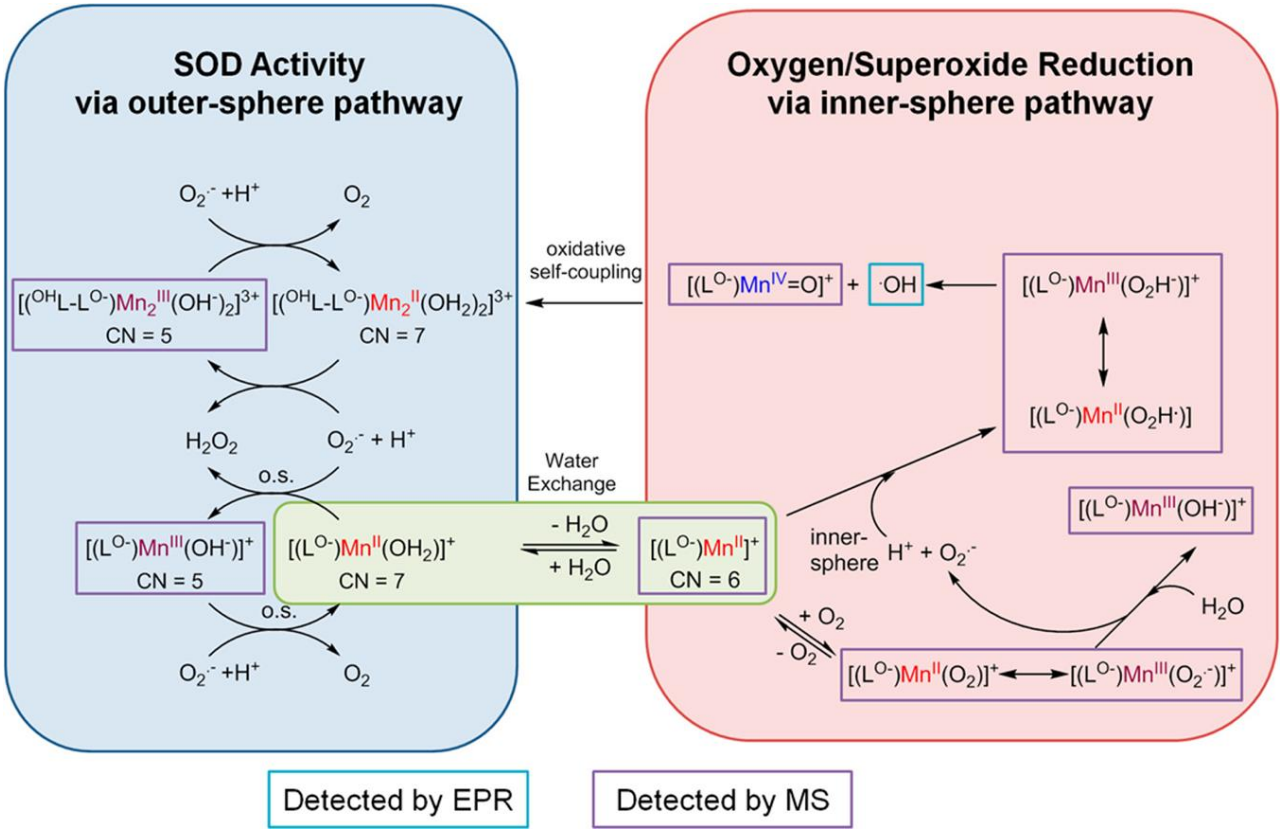

Figure 1.3: Representation of SOD and redox activity of Mn^{2+}Hptp1.[55]

The Mn^{2+} with the H_2qp1 ligand was found to also be heptacoordinate but with a distorted face-capped actahedron geometry as a mononuclear crystal. The measured relaxivity was found to be 4.73 $mM^{-1}s^{-1}$ and increased to 5.30 $mM^{-1}s^{-1}$ upon exposure to H_2O_2.[56] This was the first instance of a turn-on response to H_2O_2 by a mononuclear MRI contrast agent. The Mn^{2+} with the H_4qp2 ligand was found to also be heptacoordinate but with a simple octahedron geometry mononuclear crystal. The measured relaxivity was found to be 5.46 $mM^{-1}s^{-1}$ and increased to 7.17 $mM^{-1}s^{-1}$ upon exposure to H_2O_2.[57] The Mn^{2+} complexes with the quinol-containing ligands (H_2qp1, H_4qp2) both display enhanced *r1* in the presence of H_2O_2. The H_4qtp2 complex, however, appears to release Mn^{2+} upon oxidation due to the increase in aquation number (*q*) to 2.8 when reacted with 1 equivalent of H_2O_2.[57]

The first goal of my project is to study the Fe^{2+} and Co^{2+} complexes with Hptp1 to determine how the metal ion influences the reactivity with O_2, O_2^-, and H_2O_2, and later to study the SOD mimicry. The second goal of my project is to stabilize *T1*-weighted contrast agents by substituting COOH groups for the H_4qtp2 pyridines to yield H_6qc1, which should still be redox-active due to its two quinol groups. The complex with Mn^{2+} will be fully characterized with an interest in determining its speciation in water and its reactivity with air and H_2O_2.

References

1. Schwarz, F.; Pearce, O.; Wang, X.; Samraj, A.N.; Laubli, H.; Garcia, J.O.; Lin, H.; Fu, X.; Garcia-Bingman, A.; Secreast, P.; Romanoski, C.E.; Heyser, C.; Glass, C.K.; Hazen, S.L.; Varki, N.; Varki, A.; Gagneux, P. *eLife* **4** (2015) 1-19.
2. Zhou, C.; Huang, Y.; Przedborski, S. *Ann. N.Y. Accad. Sci.* **1147** (2008) 93-104.
3. Rimessi, A.; Previat, M.; Nigro, F.; Wieckowski, M.R.; Pinton, P. *Int. J. Biochem. Cell Biol.* **81** (2016) 281-293.
4. White, M.; Colen, J.; Humnel, C.; Burky, R.; Cruz, A.; Farias-Eisner, R. *Cancer: Oxidative Stress & Dietary Antioxidants* (2014) 41-50.
5. Paschos, A.; Pandya, R.; Duivevoorden, W.C.M.; Pinthus, J.H. *Prostate Cancer Prostatic Dis.* **16 (**2013) 217-225.
6. Yu, Z.; Sun, Q.; Pan, W.; Li, N.; Tang, B. *ACS Nano.* **9 (**2015) 11064-11074 .
7. Harrison, I.P.; Selemidis, S. *Clin. Exp. Pharmacol. Physiol.* **41** (2014) 533-542.
8. Roberts, C.K.; Sindhu, K.K. *Life Sci*. **84** (2009) 705-712.
9. Santilli, F.; D'Ardes, D.; Davi, G. *Vascul. Pharmacol.* **74** (2015) 23-37.
10. Fearon I. M., Faux S. P. *J. Mol. Cell. Cardiol***., 47** (2009) 372-381.
11. Shishehbor M. H., Aviles R. J., Brennan M. L., Fu X., Goormastic M., Pearce G. L., Gokce N., Keaney J. F., Jr., Penn M. S., Sprecher D. L., Vita J. A., Hazen S. L. *J. Am. Med. Assoc.* **289** (2003) 1675-1680.
12. Gladden J. D., Zelickson B. R., Wei C.-C., Ulasova E., Zheng J., Ahmed M. I., Chen Y., Bamman M., Ballinger S., Darley-Usmar V., Dell 'Italia L. J. *Free Rad. Biol. Med.* **51** (2011) 1975-1984.

13. Ulasova E., Gladden J. D., Chen Y., Zheng J., Pat B., Bradley W., Powell P., Zmijewski J. W., Zelickson B. R., Ballinger S. W., Darley-Usmar V., Dell'Italia L. J. *J. Mol. Cell. Cardiol.* **50** (2011) 147-156.

14. Viappiani S., Schulz R. *Am. J. Physiol. Heart Circ. Physiol.* **290** (2006) H2167-H2168.

15. Kinnula V. L. *Curr. Drug Targets. Inflamm. Allergy*, **4** (2005) 465-470.

16. Breckwoldt M. O., Chen J. W., Stangenberg L., Aikawa E., Rodriguez E., Qiu S., Moskowitz M. A., Weissleder R. *Proc. Nat. Acad. Sci., U. S. A.* **105** (2008) 18584-18589.

17. Shah, D.; Mahajan, N.; Sah, S.; Nath, S.K.; Paudyal, B. *J. of Biomedical Science* **21** (2014) 1-13.

18. Wang J.-Y., Wen L.-L., Huang Y.-N., Chen Y.-T., Ku M.-C. *Curr. Pharm. Des.* **12** (2006) 3521-3533.

19. Tretter L., Sipos I., Adam-Vizi V. *Neurochem. Res.***29** (2004) 569-577.

20. Mosley R. L., Benner E. J., Kadiu I., Thomas M., Boska M. D., Hasan K., Laurie C., *Clin. Neurosci. Res.* **6** (2006) 261-281.

21. van Horssen J., Witte M. E., Schreibelt G., de Vries H. E. *Biochim. Biophys. Acta*. **1812** (2011) 141-150.

22. Pederson, J.T.; Chen, S.W.; Borg, C.B.; Ness, S.; Bahl, J.M.; Heegaard, M.H.H.; Dobson, C.M.; Hemmingson, L.; Cremades, N.; Teilum, K. *J. Am. Chem. Soc.* **138** (2016) 3966-3969.

23. Serrano F., Klann E. *Ageing Res. Rev*.**3** (2004) 431-443.

24. Sahoo, S.; Meijiles, D.N.; Pagano, P.J. *Clin. Sci.* **130** (2016) 317-335.

25. Krohn, K. A.; Link, J. M.; Mason, R. P. *J. Nucl. Med.* **49** (2008) 129-148.

26. Jerome, N. P.; Hekmatyar, S. K.; Kauppinen, R. A. *J. of Mag. Res. Imag.*, **39** (2014) 110–119.

27. Tsitovich, P. B.; Burns, P. J.; McKay, A. M.; Morrow, J. R. *J. Inorg. Biochem.* **133** (2014) 143-154.

28. Loving, G. S.; Mukherjee, S.; Caravan, P. *J. Am. Chem. Soc.* **135** (2013) 4620– 4623.

29. Kim, B. J.; Hambley, T. W.; Bryce, N. S. *Chem. Sci*. **2 (11)** (2011) 2135–2142.

30. Brown, J. M.; Wilson, W. R. *Nature Reviews Cancer* **4 (6)** (2004) 437–447.

31. Wu, B.; Warnock, G.; Zaiss, M.; Lin, C.; Chen, M.; Zhou, Z.; Mu, L.; Nanz, D.; Tuura, R.; Delso, G. *EJNMMI Phys*, **3 (1)** (2016) https://doi.org/10.1186/s40658-016-0155-2.

32. Berger, A. *BMJ* **326 (7404)** (2003) 1449.

33. Concept :: How MRI Works :: Jeffery West Design Information Design and Illustration Visualize, Communicate, and Make Yourself Understood http://www.jwestdesign.com/concept/concept-3.html (accessed March 7, 2019).

34. Caravan, P. *Chem. Soc. Rev.* **35** (2006) 512-523.

35. Caravan P., Ellison J. J., McMurry T. J., Lauffer R. B. *Chem. Rev.* **99** (1999) 2293-2352.

36. Gale, E. M.; Zhu, J.; Caravan, P. *J. Am. Chem. Soc.* **135** (2013) 18600-186008.

37. Sherry, A. D.; Caravan, P.; Lenkinski, R. E. *J. Magn. Reson. Imaging.* **30** (2009) 1240-1248.

38. Hung, A. H.; Holbrook, R. J.; Rotz, M. W.; Glasscock, C. J.; Mansukhani, N. D.; MacRenaris, K. W.; Manus, L. M.; Duch, M. C.; Dam, K. T.; Hersam, M. C.; Meade, T. J. *ACS Nano*. **8** (2014) 10168-10177.

39. Zhang, X.-A.; Lovejoy, K. S.; Jasanoff, A.; Lippard, S. J. *Proc Natl Acad Sci U S A* **104** (2007) 10780-10785.

40. Baradov, A.; Bartelle, B.; Gonzalez, B.; White, W.; Lippard, S.; Jasanoff, A. *J. Am. Chem. Soc.* **138** (2016) 5483-5486.

41. Tsien, R. Y. A Non-Disruptive Technique for Loading Calcium Buffers and Indicators into Cells. *Nature* **290** (1981) 527-528.

42. Lord, M.L.; McNeil, F.E.; Grafe, J.L.; Noseworthy, M.D.; Chettle, D.R. *Appl. Radiat. Isot.* **112** (2016) 103-109.

43. Kanda, T.; Fukusato, T.; Matsuda, M.; Toyoda, K.; Oba, H.; Kotoku, J.; Haruyama, T.; Kitajima, K.; Furui, S. *Radiology* **276** (2015) 228-232.

44. Viger, M.L.; Sankaranarayanan, J.; de Gracia Lux, C.; Chan, M.; Almutairi, A. *J. Am. Chem. Soc.* **135** (2013) 7847-7850.

45. Gale, E. M.; Atanasova, I. P.; Blasi, F.; Ay, I.; Caravan, P.. *J. Am. Chem. Soc.* **137** (2015) 15548-15557.

46. Institute of Medicine. *Dietary Reference Intake for Vitamin A, Vitamin K, Arsenic, Boron, Chromium, Copper, Iodine, Manganese, Molybdenum, Nickel, Silicon, Vanadium, and Zinc*; National Academies Press: Washington DC, 2001.

47. Lieb, D.; Kenkell, I.; Miljkovic, J.; Moldenhauer, D.; Weber, N.; Filipovic, M.; Grohn, F.; Ivanovic-Burmazovic, I. *Inorg. Chem.* **53** (2014) 1009-1020.

48. Lieb, D.; Friedel, F.; Yawer, M.; Zahl, A.; Khusniyarov, M.; Heinemann, F.; Ivanovic-Burmazovic, I. *Inorg. Chem.* **52** (2013) 222-236.

49. Friedel, F.; Lieb, D.; Ivanovic-Burmazovic, I. *J. Inorg. Biochem.* **109** (2012) 26-32.

50. Gale, E. M.; Mukherjee, S.; Liu, C.; Loving, G. S.; Caravan, P. *Inorg. Chem.* **53** (2014) 10748–10761.

51. Gale, E. M.; Jones, C. M.; Ramsay, I.; Farrar, C. T.; Caravan, P.A. *J. Am. Chem. Soc.* **138** (2016) 15861– 15864.

52. Mathieu, E.; Bernard, A.; Delsuc, N.; Quevrian, E.; Gazzah, G.; Lai, B.; Chain, F.; Langella, P.; Bachelet, M.; Masliah, J.; Seksik, P.; Policar, C. *Inorg. Chem*. **56** (2017) 2545-2555.

53. Ching, H. Y,; Kenkel, I.; Delsuc, N.; Mathieu, E.; Ivanovic-Burmazovic, I.; Policar, C. *J. Bio. Inorg.* **160** (2016) 172-179.

54. Yu, M.; Beyers, R.; Gorden, J.; Cross, J.; Goldsmith, C. *Inorg. Chem.* **51** (2012) 9153-9155.

55. Kenkel, I.; Franke, A.; Dürr, M.; Zahl, A.; Dücker-Benfer, C.; Langer, J.; Filipović, M. R.; Yu, M.; Puchta, R.; Fiedler, S. R.; Shores, M. P.; Goldsmith, C. R.; Ivanović-Burmazović, I. *J. Am. Chem. Soc.* **139 (4)** (2017) 1472–1484.

56. Yu, M.; Ambrose, S.L.; Whaley, Z.L.; Fan, S.; Gorden, J.D.; Beyers, R.J.; Schwartz, D.D.; Goldsmith, C.R. *J. Am. Chem. Soc.* **136** (2014) 12836-12839.

57. Yu, M.; Ward, M. B.; Franke, A.; Ambrose, S. L.; Whaley, Z. L.; Bradfors, T.M.; Gorden, J. D.; Beyers, R. J.; Cattley, R.C.; Ivanovic-Burmazovic, I.; Schwartz, D.D.; Goldsmith, C.R. *Inorg. Chem.* **56** (2017) 2812-2826.

Chapter 2

Iron (II) and Cobalt (II) superoxide dismutase mimics with focus on Iron (II)

2.1 Introduction

Superoxide dismutases (SOD) is one of the human body's natural defenses against reactive oxygen species (ROS). ROSs have been known to cause a significant number of issues when there are not enough SODs to combat the rising levels of ·OH, O^{2-}, and H_2O_2.[1-7] Because of this, research and development of SOD mimics has risen. Mimics to-date include nanoparticles, use of proteins, macromolecular, and mononuclear complexes containing first row transition metals Mn^{2+}/Mn^{3+}, Fe^{2+}/Fe^{3+}, and Cu^{2+}.[8-19] The most popular of these being Mn^{2+} complexes. This research and discussion will be of mononuclear Fe^{2+} and Co^{2+} complexes as potential SOD mimics with heavier emphasis and focus on Fe^{2+} mononuclear small molecule complex (Scheme 2.1).

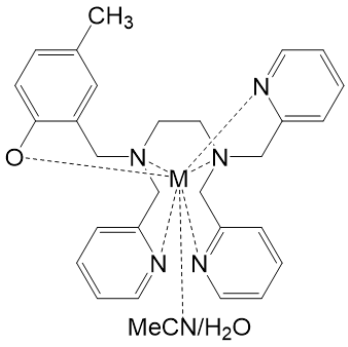

Scheme 2.1: Fe^{2+} and Co^{2+} complexes. M=Fe/Co

Structure and synthesis of these SOD mimics should include being non antigenic, low molecular weight to cross cellular membranes, low toxicity, aqueous stability, and antioxidant ability.[5,6,20,21] In order to perform as an efficient SOD mimic, the Fe^{2+} complexes are thought to function as Mn^{2+} complexes in superoxide dismutase activity (Figure 2.1).

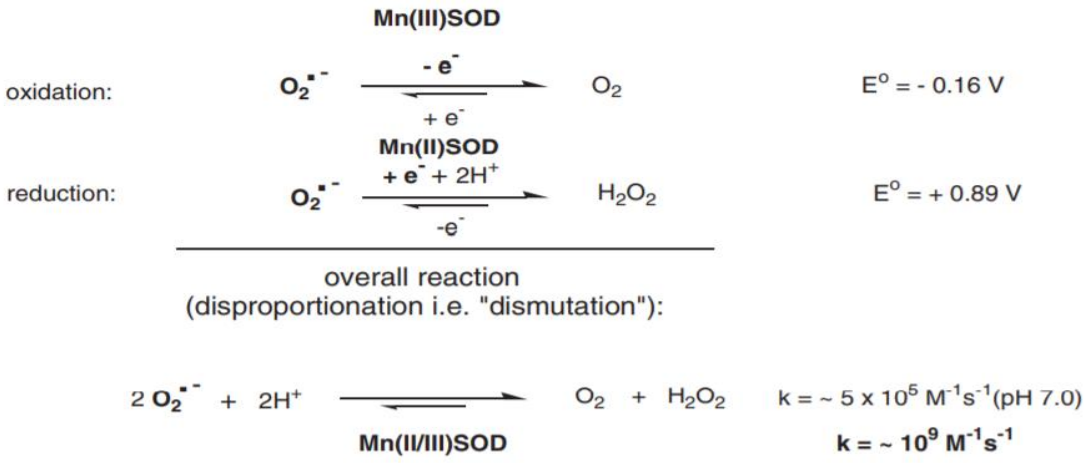

Figure 2.1: Superoxide dismutase process

Further research by the Goldsmith group in collaboration with Ivana Ivanovic-Burmazovic and group have shown inner and outer spere pathways for both oxygen/superoxide reduction and SOD activity respectively (Figure 2.2).[21]

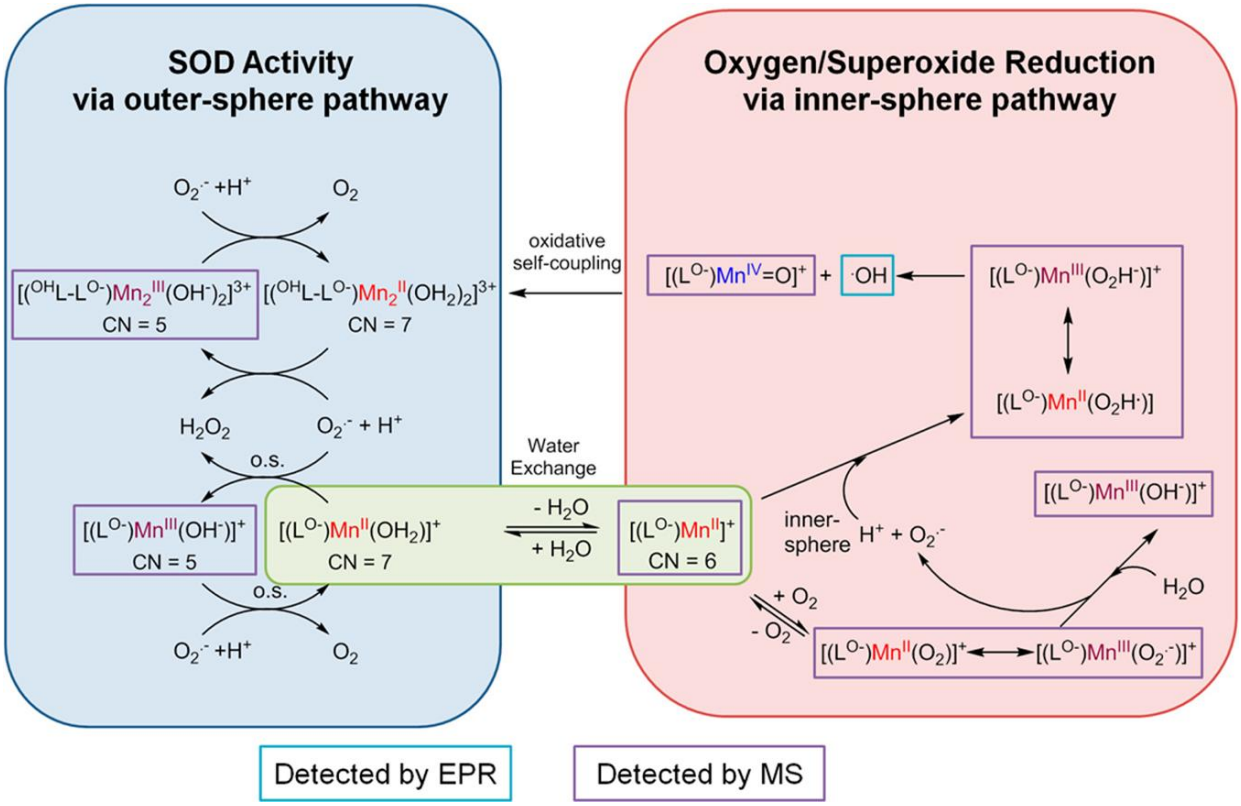

Figure 2.2: Overall reaction scheme of Mn^{2+} complex.[21]

It is believed for SOD activity to occur the mononuclear Mn^{2+} complex reacts with introduced H_2O_2 to produce the dinuclear Mn^{2+} complex. This pathway is attributed to phenol groups acting as a hydrogen atom extractor, and it thought to initially occur through water exchange.[21] This water exchange opens the door to oxygen/superoxide reduction, and through this reduction produces a Mn^{4+} complex that through self-oxidation produces the dinuclear Mn^{2+} complex. [21]

This is where the remainder of the studies for both the Fe^{2+} and Co^{2+} are to continue. It is thought that based on preliminary data the focus will held to Fe^{2+} complex and keeping the Co^{2+} complex as a standard.

2.2 Experimental Section

Materials

All chemicals were purchased from Sigma-Aldrich and used as received, unless noted otherwise. Diethyl ether (ether), ethyl acetate (EtOAc), methanol (MeOH), dichloromethane (CH_2Cl_2), and ethanol (EtOH) were bought from VWR. 1,2-Ethylenediamine was purchased from Fluka. All deuterated solvents were bought from Cambridge Isotopes and used as received.

Instrumentation

^{1}H and ^{13}C NMR spectra were recorded on either a 400 MHz or 600 MHz AV Bruker NMR spectrometer. IR spectra were collected with a Nicolet iS-50 spectrometer. Electron paramagnetic resonance (EPR) spectra were collected on a Bruker EMX-6/1 X-band EPR spectrometer operated in the perpendicular mode and analyzed with the program EasySpin. All EPR samples were run as frozen solutions in quartz tubes. High-resolution mass spectrometry (HR-MS) data were obtained at the Mass Spectrometry Center at Auburn University on a Bruker microflex LT MALDI-TOF mass spectrometer via direct probe analysis operated in the positive ion mode.

Synthesis

N-(2-Hydroxy-5-methyl-benzyl)-N,N',N'-tris(2-pyridinylmethyl)-1,2-ethanediamine (Hptp1).

This compound was prepared through a previously reported procedure.[22]

[Fe(Hptp1)(CF_3O_3S)$_2$]

The Hptp1 ligand (226 mg, 0.498 mmol) and $Fe(CF_3O_3S)_2$ (188 mg, 0.532 mmol) were dissolved in 2 mL of anhydrous MeCN and stirred under N_2 for 1 h. The mixture was then heated to a low boil while stirring under N_2 until a thin film formed. The solution was precipitated from slow addition of ether yielding a dark green powder (371 mg, 92% yield). MS (ESI): Calcd for $[Fe(Hptp1)(CF_3O_3S)]^+$, 658.1398 and for $[Fe(ptp1)]^{2+}$, 508.1800; Found, 658.0602 and 508.0850. Elemental Analysis: Calcd for $C_{28}H_{31}N_5OFeC_2F_6O_6S_2 \cdot 3H_2O$: C, 42.31%; H, 4.31%; N, 7.70%; Found: C, 41.82%; H, 4.32%; N, 8.12%. IR (KBr, cm^{-1}): 3437(s), 2365(w), 2332(w), 1605(s), 1383(s), 1352(m), 1267(m), 1160(w), 1029(s), 768(m), 640(m). UV/VIS (MeCN, 295 K): 665 nm (1400 M^{-1} cm^{-1}), 388 nm (8100 M^{-1} cm^{-1}). Solid-state magnetic susceptibility (294 K): μ_{eff} = 4.1 μ_B.

[Fe(Hptp1)$(CF_3O_3S)_2$] oxidized by air

The Hptp1 ligand (227 mg, 0.502 mmol) and $Fe(CF_3O_3S)_2$ (192 mg, 0.543 mmol) were dissolved in 5 mL of anhydrous MeCN and stirred open to air for 1 h, and solvent was removed. The resultant product was precipitated from MeCN/Ether yielding a dark blue powder (439 mg, 98% yield).

[Co(Hptp1)$(ClO_4)_2$]

The Hptp1 ligand (229 mg, 0.504 mmol) and $Co(ClO_4)_2 \cdot 6H_2O$ (181 mg, 0.494 mmol) were dissolved in 2 mL of anhydrous MeCN and stirred under N_2 for 1 h. Ether (1 mL) was added dropwise while the solution continually stirred under N_2. The resultant solution was left overnight under N_2 to deposit the product as a tan powder (309 mg, 86% yield). MS (ESI): Calcd for $[Co(Hptp1)(ClO_4)]^+$, 611.1340 and for $[Co(ptp1)]^{2+}$, 511.1777; Found, 611.0600 and 511.0901. Elemental Analysis: Calcd for $C_{28}H_{31}N_5CoCl_2O_9 \cdot 0.5H_2O$: C, 46.24%; H, 4.72%; N, 9.99%; Found: C, 46.67%; H, 4.47%; N, 9.72%. IR (KBr, cm^{-1}): 3432(s), 2359(w), 2335(w),

1607(s), 1482(m), 1436(m), 1383(m), 1352(m), 1296(w), 12589(w), 1111(s), 1083(s), 826(w), 768(m), 623(s). UV/VIS (MeCN, 295 K): λ_{max} = 451 nm (1600 M^{-1} cm^{-1}).

2.3 Results

Oxidative Characterization of [Fe(Hptp1)(CF_3O_3S)$_2$]

A series of experiments were performed for the Fe(II) complex reactivity to air, H_2O_2, and NEt_3 using UV-Vis. All samples were taken from a stock solution and diluted to 0.1mM solution. The first reaction was the O_2 reactivity solution (Figure 2.3). The [Fe(Hptp1)(CF_3O_3S)$_2$] complex (0.2 mg, 2.5 × 10^{-4} mmol) was dissolved in 6.0 mL of anhydrous MeCN. The complex was exposed to air and scans were taken every 30 min for 3 h. The maximum wavelength and extinction coefficient for the initial scan, shown in Figure 2.3 as the red line, are as follows: 665 nm, 1400 M^{-1} cm^{-1}; 388 nm, 8100 M^{-1} cm^{-1}. From the initial scan forward, the iron complex was exposed to air and likely oxidized revealing an increase in the peak at 665 nm and decreasing the peak at 388 nm. This oxidation occurs slowly overtime and shows that this iron complex is not as reactive as other iron complexes that have been designed by other researchers including Caravan and coworkers. [23-26]

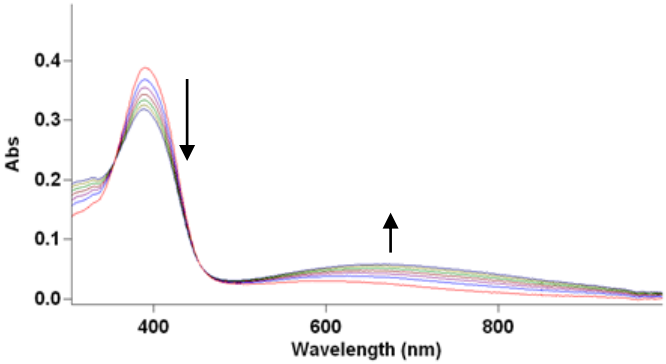

Figure 2.3: UV/VIS of [Fe(Hptp1)(CF_3O_3S)$_2$] complex (0.2 mg, 2.5 × 10^{-4} mmol) dissolved in 6.0 mL of anhydrous MeCN and exposed to air, scans taken every 30 min apart.

Once air stability was established, the second experiment was to test H_2O_2 reactivity. The $[Fe(Hptp1)(CF_3O_3S)_2]$ complex (0.2 mg, 2.5×10^{-4} mmol) and a drop of H_2O_2 (4.5 mg, 0.13 mmol) were dissolved in 6.0 mL of anhydrous MeCN. UV/VIS scans were taken every 5-10 min over 90 min as shown in Figure 2.4. The red line indicates the initial complex in solution with minimal exposure to air (less than one minute) with a peak at 395 nm. Immediately after exposure to H_2O_2 there is a reaction indicating the 395 nm peak decreasing and a peak at 336 nm beginning to form.

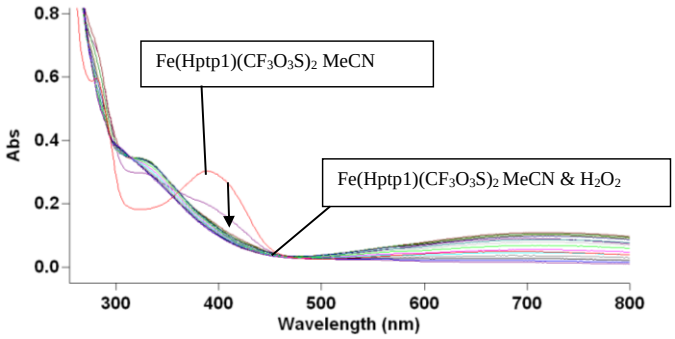

Figure 2.4: UV/VIS of $[Fe(Hptp1)(CF_3O_3S)_2]$] complex (0.2 mg, 2.5×10^{-4} mmol) and a drop of H_2O_2 (4.5 mg, 0.13 mmol) dissolved in 6.0 mL of anhydrous MeCN.

The third and fourth reactions were performed to observe what would happen when $[Fe(Hptp1)(CF_3O_3S)_2]$ complex was exposed to triethyl amine without and with hydrogen peroxide shown in Figures 2.5 and 2.6 respectively. First, the $[Fe(Hptp1)(CF_3O_3S)_2]$ complex (0.2 mg, 2.5×10^{-4} mmol) and a drop of NEt_3 (2.8 mg, 1.6×10^{-2} mmol) were dissolved in 6.0 mL of anhydrous MeCN.

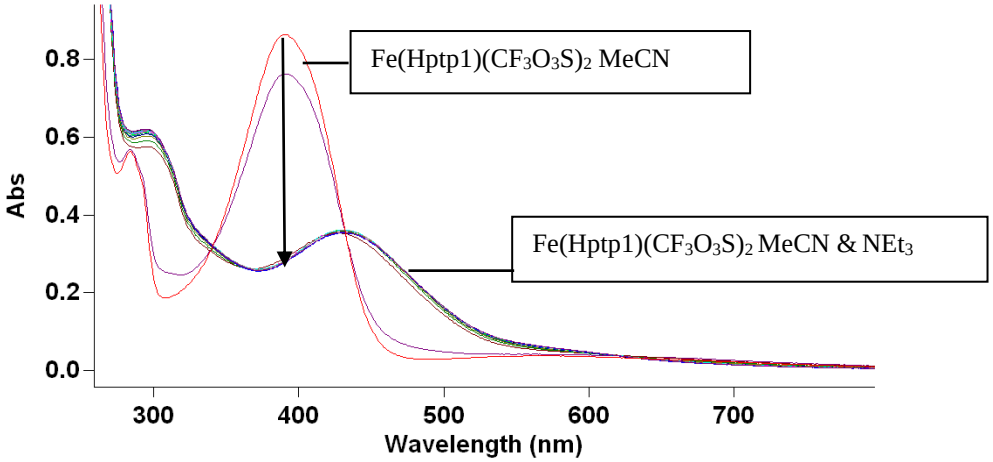

Figure 2.5: UV/VIS of $[Fe(Hptp1)(CF_3O_3S)_2]$] complex (0.2 mg, 2.5×10^{-4} mmol) and a drop of NEt_3 (2.8 mg, 1.6×10^{-2} mmol) dissolved in 6.0 mL of anhydrous MeCN.

UV/VIS scans were taken every 5 min over 60 min (Figure 2.5). During the first five minutes of the reaction there is a slight decrease in the peak at 398 nm, and after ten minutes the peak has completely shifted to 420 nm. This indicated a reaction does occur between [Fe(Hptp1)(CF_3O_3S)$_2$] complex and triethyl amine open to air. This is not simply an air reaction because as shown in Figure 1 the air reactivity of [Fe(Hptp1)(CF_3O_3S)$_2$] complex happens at a slower rate. Second, the [Fe(Hptp1)(CF_3O_3S)$_2$] complex (0.2 mg, 2.5×10^{-4} mmol), a drop of NEt_3 (2.8 mg, 1.6×10^{-2} mmol), and a drop of H_2O_2 (4.5 mg, 0.13 mmol) were dissolved in 6.0 mL of anhydrous MeCN. UV/VIS scans were taken every 30 min over 4h (Figure 2.6). Immediately after exposure to hydrogen peroxide the 398 nm peak decreases to nothing indicating a reaction did occur.

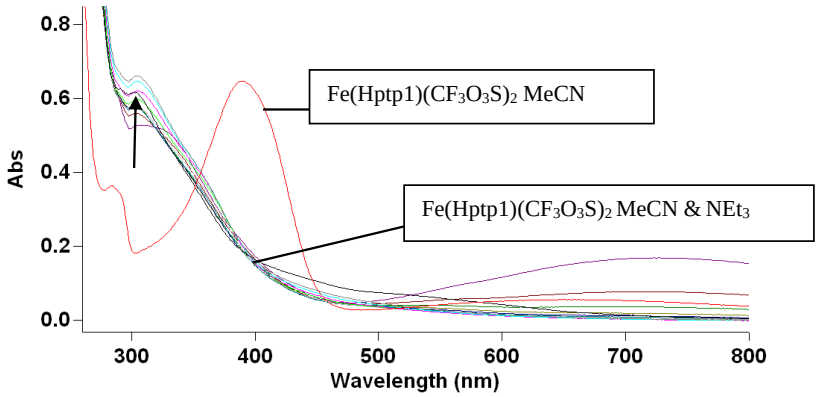

Figure 2.6: UV/VIS of [Fe(Hptp1)(CF_3O_3S)$_2$] complex (2.5×10^{-4} mmol), a drop of NEt_3 (2.8 mg, 1.6×10^{-2} mmol), and a drop of H_2O_2 (4.5 mg, 0.13 mmol) dissolved in 6.0 mL of anhydrous MeCN.

To have a standard comparison to [Fe(Hptp1)(CF_3O_3S)$_2$] complex a [Co(Hptp1)(ClO_4)$_2$] complex was also developed. This complex was placed through all the same reactions as mentioned above and can be referenced in the Appendix. Each of the reactions of [Co(Hptp1)(ClO_4)$_2$] complex had little to no reactivity at all. Next, both complexes' aqueous characterization was characterized through Electron Paramagnetic Resonance (EPR). A 1.0 mM solution of [Fe(Hptp1)(CF_3O_3S)$_2$] and anhydrous MeCN was characterized via EPR at 5 K. The first sample was 1.0 mM, MeCN, under N_2, g_{eff} = 4.28 (Figure 2.7). This figure is indicitive of a high-spin Fe(II) complex and confirms [Fe(Hptp1)(CF_3O_3S)$_2$] complex is high-spin. The second

sample was 1.0 mM, MeCN, exposed to air for 30 min, g_{eff} = 4.2, g_{eff} = 2.54, g_{eff} = 2.15, g_{eff} = 1.85 (Figure 2.8). Exposing the $[Fe(Hptp1)(CF_3O_3S)_2]$ complex to air for 30 minutes shows that a reaction does occur as seen in previously in Figure 1. Upon exposure to air, it seems the metal complex becomes a spin-crossover complex changing the oxidation state of the metal to a possible +2/+3 species. Other EPRs were taken with both $[Fe(Hptp1)(CF_3O_3S)_2]$ complex and $[Co(Hptp1)(ClO_4)_2]$ complex, and both showed no reactivity of the metals. Both remained a what is comparatively high spin complexes with no change in the oxidation state. These figures can be found in the appendix.

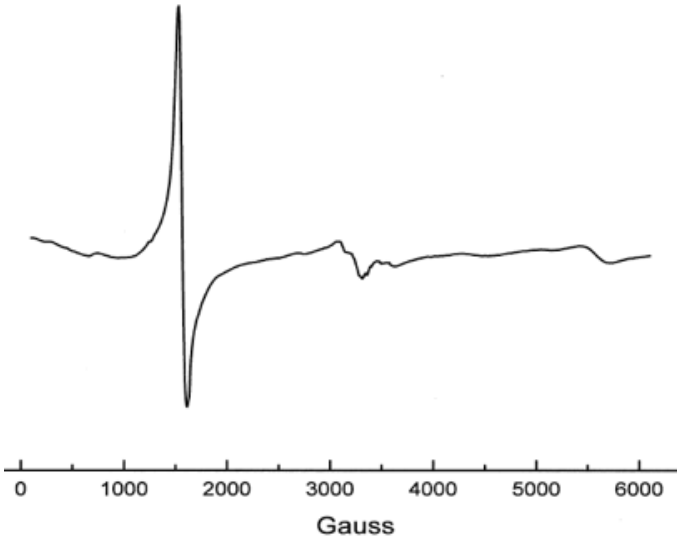

Figure 2.7: EPR of 1.0 mM solution of $[Fe(Hptp1)(CF_3O_3S)_2]$ under N_2.

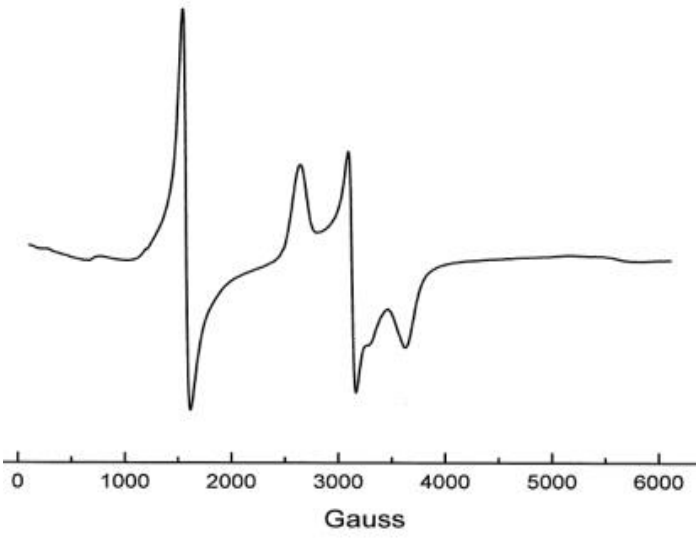

Figure 2.8: EPR of 1.0 mM solution of $[Fe(Hptp1)(CF_3O_3S)_2]$ open to air 30 min.

The speciation of Fe(II) complex with Hptp1 in water was analyzed using a 100 mM solution of KCl containing a 1:1 mixture of $FeCl_2$ and ligand by spectrophotometric titration. The pH was lowered to 2.96 using a standardized 0.1M HCl

solution. The pH was the raised slowly with a standardized solution of 0.1M KOH, and with each change of the pH a scan was taken via UV/VIS (Figure 2.9). The pH ranges of 2.96-4.03 shows some features with a slight shoulder peak at 382 nm and a ligand-metal transfer peak at 745 nm. As the pH increases the peaks shift to 440 nm and 562 nm, showing a change in the complex as the pH changes. The same was performed with the [Co(Hptp1)(ClO_4)$_2$] complex and no reactivity took place; the figure can be referenced in the appendix for comparison.

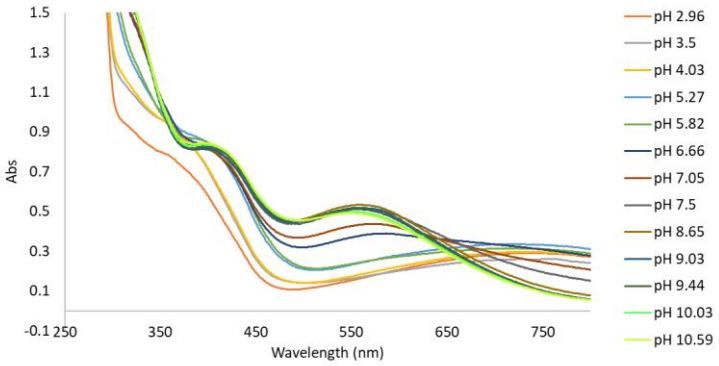

Figure 2.9: Spectrophotometric titration of [Fe(Hptp1)(CF_3O_3S)$_2$] complex.

Also tested was the Hptp1 complexes as catalysts for C-H activation and olefin epoxidation by air and H_2O_2. Cyclohexene served as the primary substrate since it can undergo both modes of reactivity. Each complex was dissolved in aerated MeCN with 1) cyclohexene, 2) cyclohexene and H_2O_2, 3) cyclohexene and NEt_3, 4) cyclohexene, H_2O_2, and NEt_3. However, no reactivity occurred for either complex, but may be performed again to check results. My lab has previously used this technique to detect the cyclohexene oxide, 2-cyclohexenol, and 2-cyclohexenone that result from epoxidation and allylic oxidation. The inner-sphere reactivity with Mn^{2+} was proposed to form Mn^{4+}-oxo species, with the oxidation of the metal becoming more favorable under basic conditions.[21] Mn^{4+}-oxo and related Fe^{4+}-oxo species are known to be powerful oxidants, capable of either C-H activation or olefin epoxidation.[27-34]

2.4 Discussion

The reaction between Fe(OTf)$_2$ and Hptp1 yields a high-spin Fe^{2+} complex, as assessed by magnetic susceptibility. It is currently unknown whether the metal center is seven-coordinate

like the Mn^{2+} ion in $[Mn(Hptp1)(MeCN)]^{2+}$. Preliminary results suggest that the compound is highly air-sensitive, even without added base (Figure 2.3). Air oxidizes the Fe^{2+} complex to a mixture of high- and low-spin Fe^{3+} species over 3 h. It is unclear as to whether the signal corresponds to two distinct products or a single spin-crossover complex. The addition of NEt_3 changes the g values associated with the low-spin signal, suggesting that the air-oxidized product may contain a protonated phenol. The oxidation can also be observed by the change in color with the initial dark green of the Fe^{2+} becoming royal blue upon oxidation to Fe^{3+}. The reactivity with H_2O_2 occurs more quickly, with most of the spectrophotometric changes happening upon mixing. Although the same color change (dark green to royal blue) is observed, the UV/VIS suggests a different product. The EPR features likewise suggest a different product since only a high-spin Fe^{3+} signal is observed. The air-sensitivity of the Fe^{2+} species suggests that inner-sphere oxygen reduction is more favorable than it is for the Mn^{2+} complex with Hptp1.

A Co^{2+} complex was prepared with Hptp1 as well. The EPR spectrum at 5 K is consistent with a high-spin Co^{2+} species. The preliminary magnetic susceptibility measurements, conversely, are consistent with a magnetic moment outside of the customary range for this ion. Although the exact composition of the complex has yet to be established, the compound is likely either $[Co(Hptp1)]^{2+}$ or $[Co(Hptp1)(MeCN)]^{2+}$, with a κ-5 Hptp1 ligand, in MeCN solution. Preliminary results demonstrate that the Co-Hptp1 complex is far less reactive (Figures S2.8, S2.9). The only experiment that resulted in observable color change is shown in Figure S2.8; the solution changed from a green to a brown/champagne color. The color change is thought to result from deprotonation of the phenol, rather than oxidation of either the ligand or metal ion. Due to the slow oxidative change of the cobalt complex, it is thought that oxygen reduction via an inner pathway and SOD activity is far slower than that of the manganese or iron complexes.

Characterization by EPR agrees with the spectrophotometric data taken. The reduced Fe^{2+} complex does show a signal at g = 4.28, however, this is a very small signal and may result from trace impurities in the instrument. The second sample of iron complex that was exposed to air for 30 min have a g value of 4.2 at relatively the same signal height as the first example. However, additional g values of 2.54, 2.15, and 1.85 were also present, suggesting that a low-spin Fe^{3+} species is in solution. Once the iron sample was exposed to H_2O_2 there was a g value reported at 4.28 with a doubled signal height, suggesting oxidation from high-spin Fe^{2+} to high-spin Fe^{3+} species. The reduced Co^{2+} complex gave a g value of 4.39 at a high signal peak. Further characterization of the Co^{2+} /Co^{3+} complex by EPR will be performed. The same EPR experiments performed for the Fe^{2+} complex will be done for the Co^{2+} complex. This will allow insight into the Co^{2+} metal center to determine if metal centered oxidation occurs. As reference guides, both iron and cobalt oxidized complexes will undergo the same analyses. If EPR shows that there is metal centered oxidation occurring, the ligand will be isolated and analyzed via NMR and MS to determine if the ligand also undergoes oxidation or any structural changes.

2.5 Proposed Future Work

Future work for the iron and cobalt complexes will include repeating the magnetic susceptibility experiments and collecting structural data. The Co^{2+} complex had a higher μ_{eff} value than expected, necessitating further characterization. The UV/VIS and EPR data for the iron complex suggest that oxidation preferentially occurs on the metal rather than the ligand. To view the oxidative state of the ligand, extraction and characterization of the ligand will be done. To do this, Fe-Hptp1 will be dissolved in MeCN with H_2O_2. Once full oxidation has occurred, EDTA will then be added to strip the iron from the Hptp1 ligand. The Hptp1 ligand will then be collected and characterized with ^1H NMR and mass spectrometry to determine whether the

ligand couples through the phenol groups, as was observed in the Mn^{2+} reactivity. The same aforementioned procedure will be performed for Co-Hptp1 as well; both oxidized and reduced complexes are currently in progress. Crystallization of both oxidized complexes is being attempted in a few different experimental pathways: first is by slow diffusion of ethyl either into a MeCN solution, and second is by slow evaporation of single solvent MeCN. The crystals that have been grown thus far are micro-crystalline and do not diffract well. If crystals cannot be grown, magnetic circular dichroism (MCD) is being considered as a viable alternative means to obtain the iron(II) complex structure.

We are also interested in determining the SOD activity of the Fe^{2+} and Co^{2+} complexes but are not equipped to do the necessary kinetic measurements at Auburn. The SOD activity will be studied using stopped-flow techniques through a collaboration with Ivana Ivanovic-Burmazovic.

Appendix 1

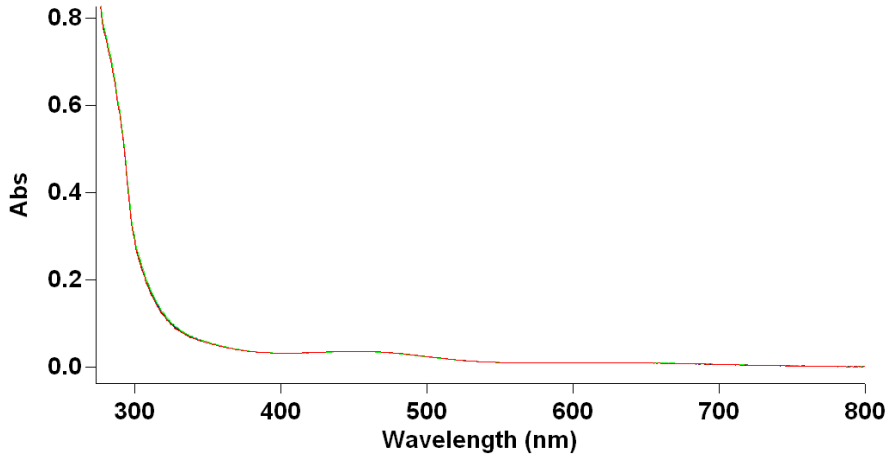

Figure S2.1: UV/VIS of [Co(Hptp1)(ClO_4)$_2$] complex (0.2 mg, 2.8 × 10^{-4} mmol) dissolved in 6.0 mL of anhydrous MeCN.

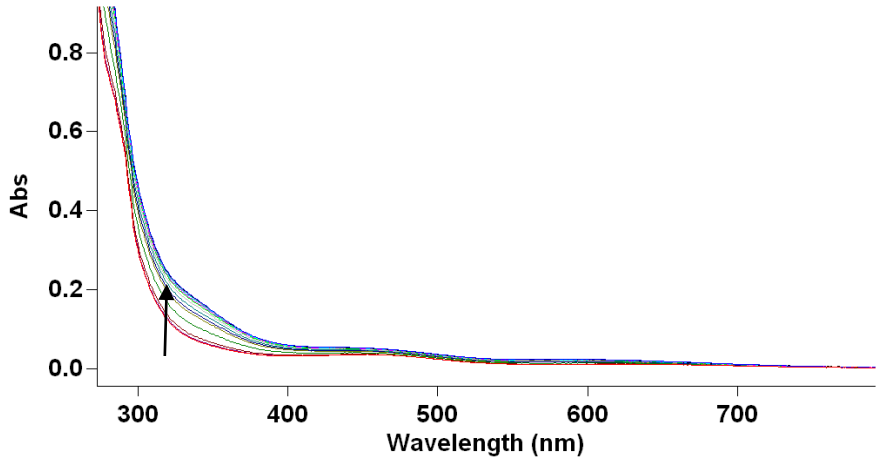

Figure S2.2: UV/VIS of [Co(Hptp1)(ClO_4)$_2$] complex (0.2 mg, 2.8x10^{-4} mmol) and a drop of H_2O_2 (4.5 mg, 0.132 mmol) dissolved in 6.0 mL of anhydrous MeCN.

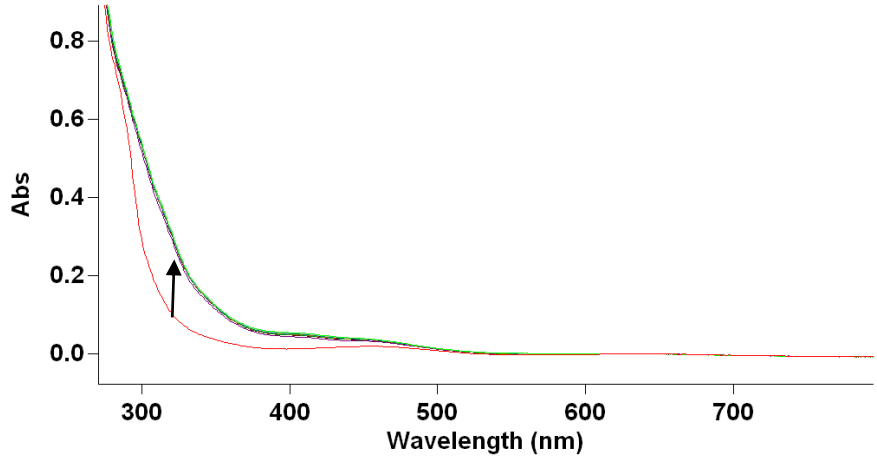

Figure S2.3: UV/VIS of [Co(Hptp1)(ClO_4)$_2$]] complex (0.2 mg, 2.81 × 10^{-4} mmol) and a drop of NEt_3 (2.8 mg, 1.62 × 10^{-2} mmol) dissolved in 6.0 mL of anhydrous MeCN.

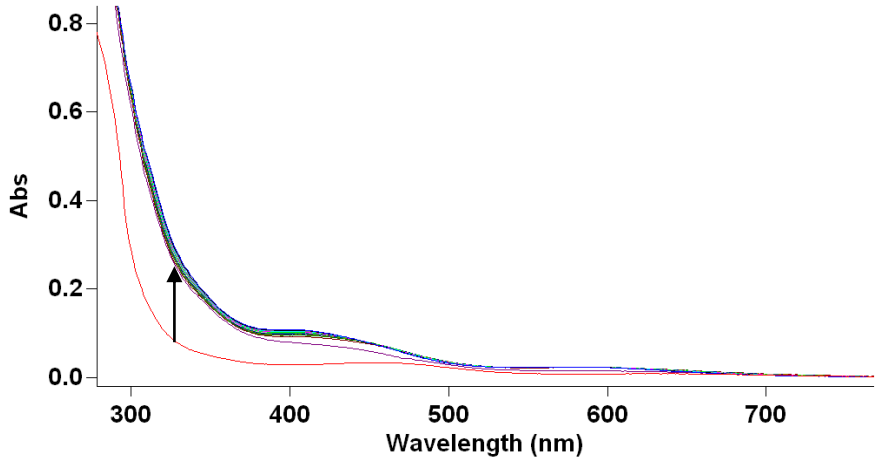

Figure S2.4: UV/VIS of [Co(Hptp1)(ClO_4)$_2$] complex (0.2 mg, 2.81 × 10^{-4} mmol), a drop of NEt_3 (2.8 mg, 1.62 × 10^{-2} mmol), and a drop of H_2O_2 (4.5 mg, 0.13 mmol) dissolved in 6.0 mL of anhydrous MeCN.

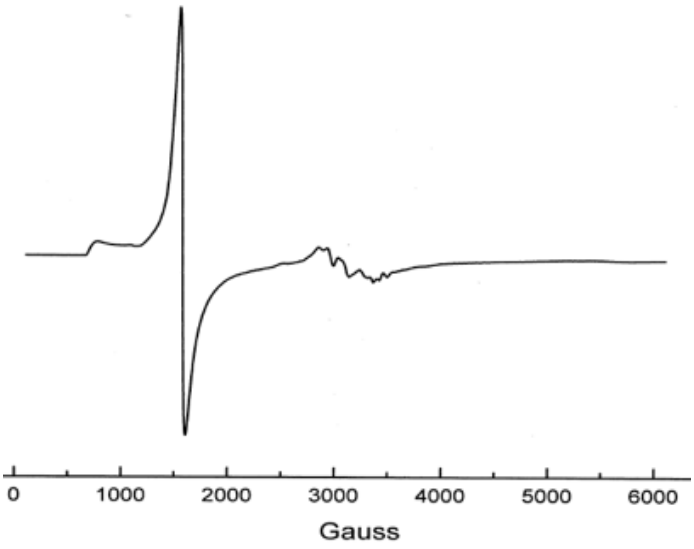

Figure S2.5: EPR of 1.0 mM solution of [Fe(Hptp1)(CF_3O_3S)$_2$] with H_2O_2 open to air for 30 min.

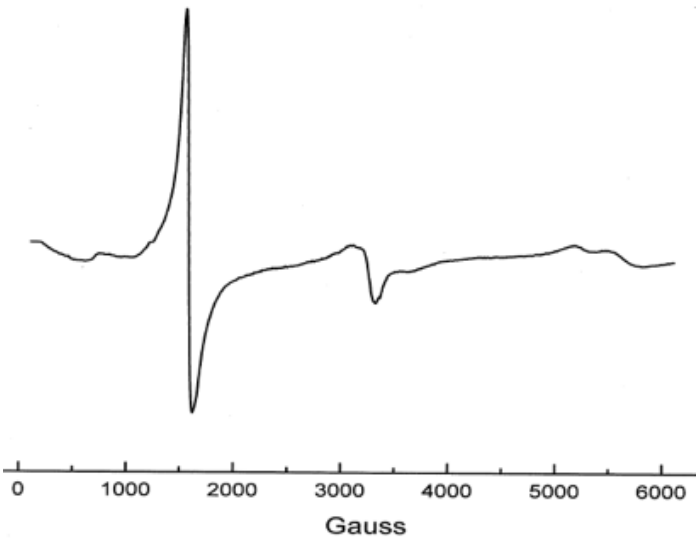

Figure S2.6: EPR of 1.0 mM solution of [Fe(Hptp1)(CF_3O_3S)$_2$] with NEt_3 open to air 30 min.

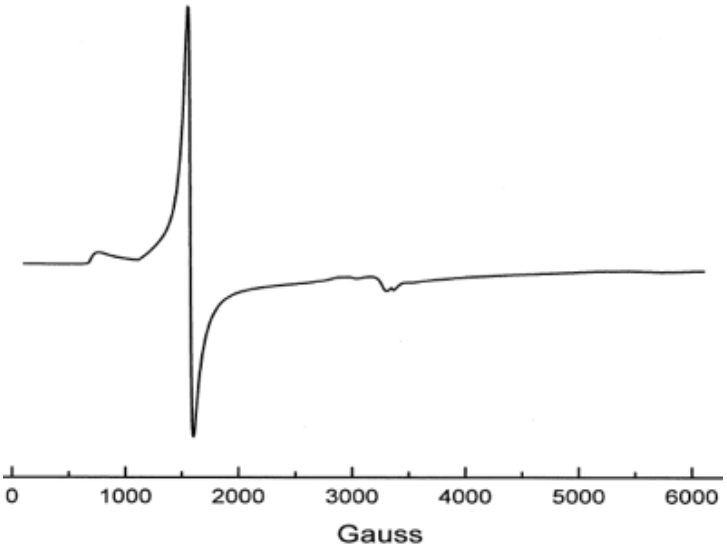

Figure S2.7: EPR of 1.0 mM solution of [Fe(Hptp1)(CF_3O_3S)$_2$] with NEt_3 and H_2O_2 open to air 30 min.

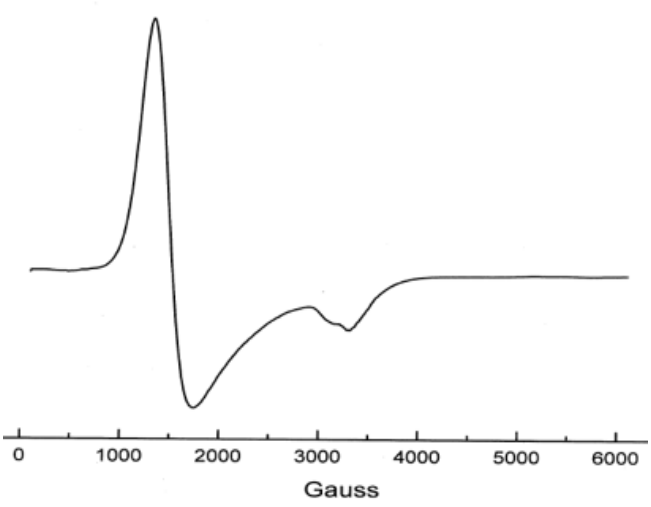

Figure S2.8: EPR of 1.0 mM solution of [Co(Hptp1)(ClO_4)$_2$] under N_2.

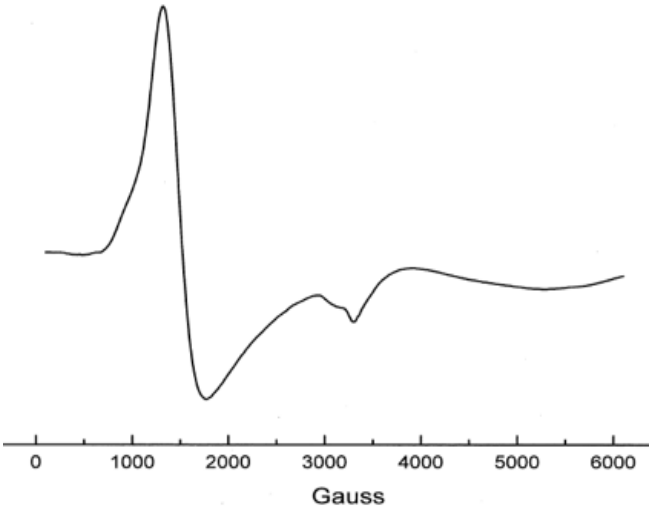

Figure S2.9: EPR of 1.0 mM solution of [Co(Hptp1)(ClO_4)$_2$] with NEt_3 under N_2.

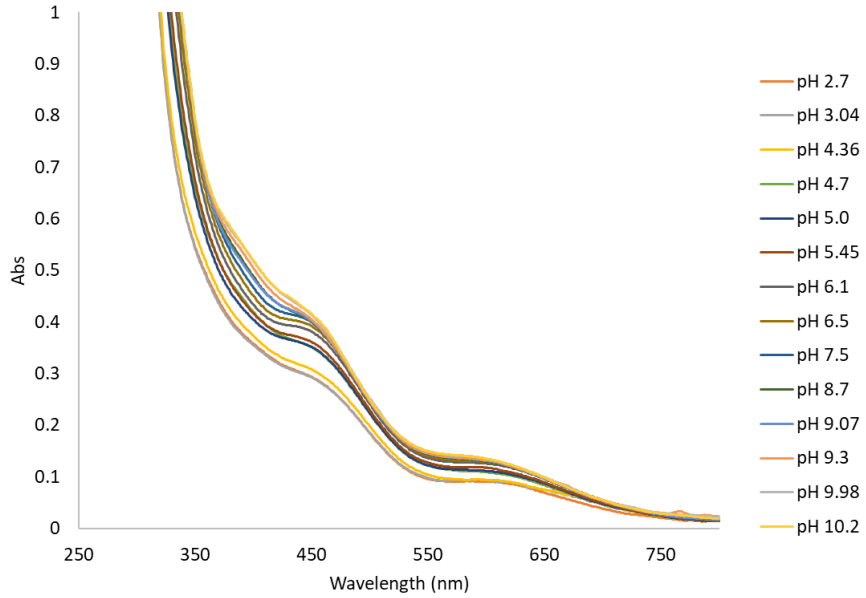

Figure S2.10: Spectrophotometric titration of $[Co(Hptp1)(ClO_4)_2]$ complex.

References

1. Giorgi, C.; Marchi, S.; Simoes, I. C. M.; Ren, Z.; Morciano, G.; Perrone, M.; Patalas-Krawczyk, P.; Borchard, S.; Jędrak, P.; Pierzynowska, K.; Szymański, J.; Wang, D. Q.; Portincasa, P.; Węgrzyn, G.; Zischka, H.; Dobrzyn, P.; Bonora, M.; Duszynski, J.; Rimessi, A.; Karkucinska-Wieckowska, A.; Dobrzyn, A.; Szabadkai, G.; Zavan, B.; Oliveira, P. J.; Sardao, V. A.; Pinton, P.; Wieckowski, M. R.. In *International Review of Cell and Molecular Biology*; López-Otín, C., Galluzzi, L., Eds.; Mitochondria and Longevity; Academic Press, **340** (2018) 209–344.
2. Miriyala, S.; Spasojevic, I.; Tovmasyan, A.; Salvemini, D.; Vujaskovic, Z.; St. Clair, D.; Batinic-Haberle, I., *Biochimica et Biophysica Acta (BBA) - Molecular Basis of Disease*, **1822 (5)** (2012) 794–814.
3. Garza-Lombó, C.; Pappa, A.; Panayiotidis, M. I., *Mitochondrion*, **51** (2020) 105–117.
4. Yang, S.; Lian, G., *Mol Cell Biochem* (2019).
5. Batinić-Haberle, I.; Rebouças, J. S.; Spasojević, I., *Antioxid Redox Signal*, **13 (6)** (2010) 877–918.
6. Superoxide dismutases: Ancient enzymes and new insights | Elsevier Enhanced Reader https://reader.elsevier.com/reader/sd/pii/S0014579311008271?token=3ABEFCFCB36312E73641C34A99502FACE1B9D57396EDD6AB650CEFEBDA5CD914D9A6958D80EEDD135818265CFACBFAA1 (accessed Aug 26, 2019). https://doi.org/10.1016/j.febslet.2011.10.048.
7. Kalyanaraman, B.; Cheng, G.; Hardy, M.; Ouari, O.; Bennett, B.; Zielonka, J., *Redox Biology*, **15** (2018) 347–362.
8. Ge, X.; Li, Z.; Yuan, Q., *Journal of Materials Science & Technology*, **31 (6)** (2015) 645–654.

9. Sakurai, Y.; Anzai, I.; Furukawa, Y., *J. Biol. Chem.*, **289 (29)** (2014) 20139–20149.
10. Venerini, F.; Sette, M.; Stroppolo, M. E.; De Martino, A.; Desideri, A., *Archives of Biochemistry and Biophysics*, **366 (1)** (1999) 70–74.
11. Kripli, B.; Baráth, G.; Balogh-Hergovich, É.; Giorgi, M.; Simaan, A. J.; Párkányi, L.; Pap, J. S.; Kaizer, J.; Speier, G., *Inorganic Chemistry Communications*, **14 (1)** (2011) 205–209.
12. Saqib, M.; Qi, L.; Hui, P.; Nsabimana, A.; Halawa, M. I.; Zhang, W.; Xu, G., *Biosensors and Bioelectronics*, **99** (2018) 519–524.
13. Güner, S.; Karaböcek, S.; Kaklikkaya, I., *Bioorganic & Medicinal Chemistry*, **7 (2)** (1999) 329–333.
14. Batinić-Haberle, I.; Spasojević, I.; Stevens, R. D.; Hambright, P.; Neta, P.; Okado-Matsumoto, A.; Fridovich, I., *Dalton Trans.* **11** (2004) 1696–1702.
15. Renault, J. P.; Verchère-Béaur, C.; Morgenstern-Badarau, I.; Piccioli, M., *FEBS Letters*, **401 (1)** (1997) 15–19.
16. Gutman, C. T.; Brunold, T. C., *Inorg. Chem.* **51 (23)**, 12729–12737 (2012).
17. Tamura, M.; Urano, Y.; Kikuchi, K.; Higuchi, T.; Hirobe, M.; Nagano, T., *Journal of Organometallic Chemistry*, **611 (1)** (2000) 586–592.
18. Sette, M.; Paci, M.; Desideri, A.; Rotilio, G., *Eur J Biochem*, **213 (1)** (1993) 391–397.
19. Xiao, H.; Zhang, W.; Li, P.; Zhang, W.; Wang, X.; Tang, B. *Angewandte Chemie International Edition*. https://doi.org/10.1002/anie.201906793.
20. Tsitovich, P. B.; Burns, P. J.; McKay, A. M.; Morrow, J. R. *J., Inorg. Biochem.* **133** (2014) 143-154.

21. Kenkel, I.; Franke, A.; Dürr, M.; Zahl, A.; Dücker-Benfer, C.; Langer, J.; Filipović, M. R.; Yu, M.; Puchta, R.; Fiedler, S. R.; Shores, M. P.; Goldsmith, C. R.; Ivanović-Burmazović, I., *J. Am. Chem. Soc.* **139 (4)** (2017) 1472–1484.

22. Meng Yu, Ronald J. Beyers, John D. Gorden, Justin N. Cross, and Christian R. Goldsmith. *Inorg. Chem*. **51 (17)** (2012) 9153-9155.

23. Huan Wang, Veronica Clavijo Jordan, Ian A. Ramsay, Mozhdeh Sojoodi, Bryan C. Fuchs, Kenneth K. Tanabe, Peter Caravan, and Eric M. Gale. *J. Am. Chem. Soc.* **141 (14)** (2019) 5916-5925.

24. Snyder, E. M.; Asik, D.; Abozeid, S. M.; Burgio, A.; Bateman, G.; Turowski, S. G.; Spernyak, J. A.; Morrow, J. R., *Angewandte Chemie*. **132 (6)** (2020) 2435–2440.

25. Bond, C. J.; Sokolow, G. E.; Crawley, M. R.; Burns, P. J.; Cox, J. M.; Mayilmurugan, R.; Morrow, J. R., *Inorg. Chem*. **58 (13)** (2019) 8710–8719.

26. Tsitovich, P. B.; Gendron, F.; Nazarenko, A. Y.; Livesay, B. N.; Lopez, A. P.; Shores, M. P.; Autschbach, J.; Morrow, J. R., *Inorg. Chem*. **57 (14)** (2018) 8364–8374.

27. Oloo, W.N.; Que Jr., L., *Acc. Chem. Res*. **48** (2015) 2612-2621.

28. England, J.; Prakash, J.; Cranswick, M.A.; Mandal, D.; Guo, Y.; Munck, E.; Shaik, S.; Que Jr., L., *Inorg. Chem*. **54** (2015) 7828-7839.

29. Kleespies, S.T.; Oloo, W.N.; Mukherjee, A.; Que Jr., L, *Inorg. Chem*. **54** (2015) 5053-5064.

30. Baglia, R.A.; Krest, C.M.; Yang, T.; Leeladee, P.; Goldberg, D.P., *Inorg. Chem*. **55** (2016) 10800-10809.

31. Sahu, S.; Goldberg, D. P., *J. Am. Chem. Soc*. **138** (2016) 11410-11428.

32. Yosca, T.H.; Langston, M.C.; Krest, C.M.; Onderko, E.L.; Grove, T.L.; Livada, J.; Green, M. T., *J. Am. Chem. Soc*. **138** (2016) 16016-16023.

33. Chang, W.; Li, J.; Lee, J.L.; Cronican, A.A.; Guo, Y., *J. Am. Chem. Soc*. **138** (2016) 10390-10393.

34. Park, J.; Lee, Y.; Ohkubo, K.; Nam, W.; Fukuzumi, S., *Inorg. Chem*. **54** (2015) 5806-5812.

Chapter 3

An Overly Anionic Metal Coordination Environment Eliminates the *T1*-Weighted Response of Quinol-Containing MRI Contrast Agent Sensors to H_2O_2*

*This Chapter is a revision of a published paper:

3.1 Introduction

The over-production of reactive oxygen species (ROS) has been associated with a wide range of health disorders, including several cardiovascular and neurological diseases.[1-5] The roles of ROS in these pathologies, however, have not been fully clarified. Being able to identify when and where ROS concentrations spike during disease progression could provide more effective means to both diagnose and treat these conditions. Spatiotemporal patterns of oxidative stress in the brain could, for instance, help to differentiate neurological conditions that give rise to similar clinically observable symptoms. In order to identify these and similar patterns, one needs a redox-active sensor that can reliably function *in vivo*. Probes that alter how tissues and organs appear when visualized by magnetic resonance imaging (MRI) are attractive in that such imaging can be done in a non-invasive manner.

Our laboratory has previously reported a series of redox-responsive contrast agents for MRI.[6-8] Our general strategy has been to complex a redox-active organic ligand to a Mn(II) ion. The high paramagnetism of high-spin Mn(II) (S = 5/2) results in a high *T1*-weighted relaxivity (*r1*). The redox activity of manganese allows it to catalyze the oxidation of the organic component by a ROS. Our more recent work has focused on using polydentate ligands with quinols as the redox-active moieties.[7, 8] Transition metal ion-catalyzed oxidation by H_2O_2 converts these to *para*-quinones (Scheme 3.1), which are more readily displaced by water molecules. The greater aquation increases *r1*, improving MRI contrast, and a ligand with two quinols, H_4qp2 (Scheme 3.2), provides a larger response.[8]

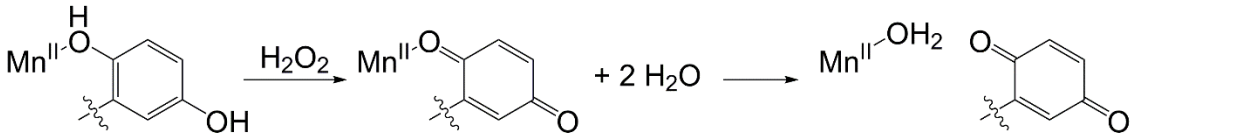

Scheme 3.1. Note that this graphic originally appeared in reference [8]

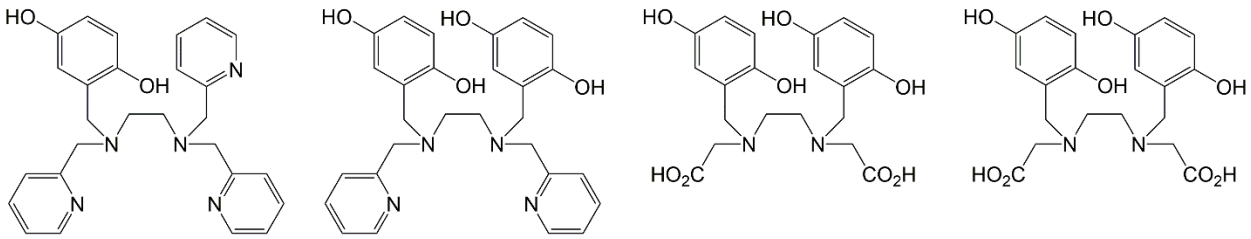

Scheme 3.2

The disadvantage of this strategy is that the oxidized ligand necessarily has a weaker binding affinity for Mn(II). Indeed, the reaction between H_2O_2 and [Mn(H_4qp2)Br_2] likely releases a substantial amount of Mn(II), based on the relatively low stability of the pre-oxidized complex and the 2.8 aquation number (q) measured for the oxidized mixture.[8] The measured q is likely elevated by the presence of $[Mn(H_2O)_6]^{2+}$ (q = 6), but the partial oxidation of the quinols prevented us from more definitively assessing the stabilities of the oxidized products. Approximately 70% of the quinols are oxidized with excess H_2O_2; this results in a mixture of Mn(II) complexes with unreacted H_4qp2, a partially oxidized ligand with only one *para*-quinone (H_2qp2), and the fully oxidized ligand with two *para*-quinones (qp2). The loss of Mn(II) from the probe is problematic for *in vivo* applications since free Mn(II) is known to be toxic.[9]

In the current work, we attempt to eliminate oxidation-triggered release of Mn(II) by substituting carboxylate groups for the pyridines in H_4qp2. Although such a substitution could be expected to lower the thermodynamic barrier for the oxidation of Mn(II) to Mn(III), Caravan's group had recently used phenol- and carboxylate-containing ligands to produce Mn(II)

complexes that are sufficiently stable to air for use as MRI contrast agents.[10-12] Further, the resulting ligand would have a strong resemblance to *N,N'*-bis(2-hydroxybenzyl)ethylenediamine-*N,N'*-diacetic acid (HBED, Scheme 2), which was synthesized and characterized by Martell and co-workers and forms a stable complex with Mn(II).[13, 14] Additionally, we have observed that a sufficiently redox-active ligand can direct redox chemistry away from the metal ion by serving as a sacrificial oxidant or reductant.[15]

We synthesized *N,N'*-bis(2,5-dihydroxybenzyl)ethanediamine-*N,N'*-diacetic acid (H_6qc1, Scheme 2) as a new hexadentate ligand. This molecule retains the two quinols of H_4qp2 that are essential to the large H_2O_2 response of its Mn(II) complex but replaces the pyridines with carboxylic acids, which readily deprotonate to carboxylate anions above pH 5.0. The installation of the carboxylic acids is anticipated to improve the binding affinity of the ligand by providing a more anionic coordination environment for cationic metal ions at ambient pH. The ligand is otherwise similar to H_4qp2; this enables us to focus on determining how ligand charge impacts the stability of the sensor and its response to H_2O_2.

3.2 Experimental Section

Materials

All chemicals were purchased from Sigma-Aldrich and used as received, unless noted otherwise. Diethyl ether (ether), ethyl acetate (EtOAc), methanol (MeOH), dichloromethane (CH_2Cl_2), and ethanol (EtOH) were bought from VWR. 1,2-Ethylenediamine was purchased from Fluka. All deuterated solvents were bought from Cambridge Isotopes and used as received.

Instrumentation

^{1}H and ^{13}C NMR spectra were recorded on either a 400 MHz or 600 MHz AV Bruker NMR spectrometer. IR spectra were collected with a Nicolet iS-50 spectrometer. Electron

paramagnetic resonance (EPR) spectra were collected on a Bruker EMX-6/1 X-band EPR spectrometer operated in the perpendicular mode and analyzed with the program EasySpin. All EPR samples were run as frozen solutions in quartz tubes. High-resolution mass spectrometry (HR-MS) data were obtained at the Mass Spectrometry Center at Auburn University on a Bruker microflex LT MALDI-TOF mass spectrometer via direct probe analysis operated in the positive ion mode.

Magnetic Resonance Imaging (MRI)

All MRI data were collected at the Auburn University MRI Research Center on a Siemens Verio open-bore 3-T MRI clinical scanner; a 15-channel knee coil was used to simultaneously image 12-15 samples. The imaging procedure was identical to those used for similar studies from our laboratory.[6-8, 16] An inversion recovery (IR) sequence was used that featured a non-selective adiabatic inversion pulse followed by a slice-selective gradient recalled echo (GRE) readout after a delay period corresponding to the inversion time (TI).[17, 18] The GRE was a saturation readout, such that only one line of k-space was acquired per repetition time (TR), in order to maximize both signal strength and the accuracy of the *T1* estimates. The specific imaging parameters were as follows: TR was set to 4 s, TI was varied from 4.8 to 2500 ms over 37 steps, the echo time (TE) was set to 3.6 ms, the flip angle equaled 90°, averages = 1, slice thickness = 5 mm, field of view = 140 × 140 mm, matrix = 128 × 128, resulting in a pixel size of 1.1 × 1.1 × 5.0 mm. All samples were run in 50 mM solutions of HEPES in water, buffered to pH 7.0 and kept at 22 °C. The manganese content was systematically varied from 0.10 to 1.00 mM. The inverses of the *T1* values were plotted versus the concentration of Mn(II) to obtain *r1* values.

MRI Data Analysis

Image analysis was performed using custom Matlab programs (Mathworks, Natick, MA). The initial TI = 4.8 ms image was used as a baseline to determine circular region of interest (ROI) boundaries for each sample; from these, the mean pixel magnitudes for each ROI were calculated. For each of the 36 subsequent TI images, the same ROI boundaries were applied, and the mean pixel magnitude calculations were repeated. This gave consistent ROI spatial definitions and a corresponding time course of magnitudes for each of the samples over all the TI time points. Each sample's complex phase was used to correct the magnitude polarity to produce a complete exponential *T1* inversion recovery curve. The Nelder-Mead simplex algorithm[19] was applied to each sample's exponential curve to estimate its corresponding *T1* value.

Synthesis

2,5-Bis(*tert*-butyldimethylsiloxy)benzaldehyde (1).

This compound was prepared through a previously reported procedure.[20] 2,5-Dihydroxybenzaldehyde (700 mg, 5.07 mmol) and imidazole (1.04 g, 15.2 mmol) were dissolved in 10 mL of anhydrous *N*,*N*-dimethylformamide under a N_2 atmosphere. The resultant solution was then cooled to 0 °C using an ice bath. *tert*-Butyldimethylsilyl chloride (1.90 g, 12.6 mmol) was added, and the reaction mixture stirred and warmed to room temperature (RT) over the next 16 h. 100 mL of water were then added to quench the reaction, and the crude product was extracted with three 50 mL portions of EtOAc. The organic layers were combined, washed with three 100 mL aliquots of water, and dried over sodium sulfate. After the EtOAc was removed by rotavaporation, the product was purified by column chromatography using 50:1 hexanes/EtOAc as the eluent (R_f = 0.2) to yield 1.60 g of the product as a yellow oil (85% yield). ^{1}H NMR (400 MHz, $CDCl_3$, 293 K): δ 10.39 (s, 1H), 7.24 (m, 1H), 6.97 (m, 1H), 6.76 (m, 1H), 1.02 (s, 9H), 0.98 (s, 9H), 0.25 (s, 6H), 0.19 (s, 6H). ^{13}C NMR (100 MHz, $CDCl_3$, 293 K): 189.9, 153.4,

149.8, 127.9, 127.4, 121.2, 117.7, 25.7, 25.6, 18.3, 18.1, -4.4, -4.5. MS (ESI): Calcd for MH^+, 367.2125; Found, 367.1879. IR (cm^{-1}): 2955.36 (m), 2930.04 (m), 2886.00 (w), 2857.88 (m), 1686.29 (m), 1608.23 (w), 1485.10 (s), 1419.96 (m), 1387.18 (m), 1362.25 (w), 1300.30 (w), 1253.61 (s), 1209.72 (s), 1150.68 (s), 1006.29 (w), 983.85 (m), 909.32 (s), 836.98 (s), 821.89 (s), 805.21 (s), 777.97 (s), 732.67 (w), 684.67 (m), 668.07 (w), 640.88 (w), 611.26 (w), 581.31 (w), 537.82 (w), 449.69 (w).

***N,N'*-Bis[2,5-bis(*tert*-butyldimethylsiloxy)benzyl]-1,2-ethanediamine (2).**

2,5-Bis(*tert*-butyldimethylsiloxy)benzaldehyde (1.10 g, 3.00 mmol) and ethylenediamine (90 mg, 1.50 mmol) were dissolved in 20 mL of dry MeOH and stirred for 16 h under N_2 at RT. ^1H NMR analysis of an aliquot taken at this time indicated that the aldehyde was fully consumed. The mixture was then cooled to 0 °C with an ice bath. Sodium borohydride (153 mg, 4.05 mmol) was added to the cooled solution, and the resultant mixture was stirred for 5 h. The MeOH was then stripped from the solution, and the crude product was dissolved in CH_2Cl_2. The crude product was washed with three portions of saturated $NaHCO_3$. Additional product was extracted from the washes with CH_2Cl_2, after which all the organic layers were combined. After the solution was dried over sodium sulfate, the CH_2Cl_2 was removed to yield the product as a yellow/brown oil (1.10 g, 75% yield). ^1H NMR (400 MHz, $CDCl_3$, 293 K): δ 6.70 (d, J = 3.2 Hz, 2H), 6.58 (m, 4H), 3.69 (s, 4H), 2.71 (s, 4H), 0.98 (s, 18H), 0.97 (s, 18H), 0.19 (s, 12H), 0.16 (s, 12H). ^{13}C NMR (100 MHz, $CDCl_3$, 293 K): δ 149.37, 147.89, 131.51, 121.33, 118.85, 118.5, 49.34, 48.76, 25.84, 25.74, 18.17, 18.15, -4.16, -4.43. MS (ESI): Calcd for MH^+, 761.4960; Found, 761.4390. IR (cm^{-1}): 2954.75 (m), 2928.86 (m), 2885.76 (w), 2857.11 (m), 1490.24 (s), 1471.75 (m), 1418.47 (w), 1399.57 (w), 1361.42 (w), 1251.29 (s), 1222.56 (s), 1156.34 (w),

1094.93 (w), 982.76 (w), 910.63 (s), 835.60 (s), 799.82 (s), 776.11 (s), 684.52 (m), 666.23 (w), 585.37 (w), 449.33 (w).

_N,N'_-Bis[2,5-bis(_tert_-butyldimethylsiloxy)benzyl]-_N,N'_-bis(_tert_-butyl-acetate)-1,2–ethanediamine (3).

_N,N'_-Bis[2,5-bis(_tert_-butyldimethylsiloxy)-benzyl]-1,2-ethanediamine (1.10 g, 1.44 mmol), _tert_-butylbromoacetate (676 mg, 3.47 mmol) and _N,N'_-diisopropylethylamine (467 mg, 3.61 mmol) were dissolved in 35 mL of CH_2Cl_2 and stirred for 24 h. The solution was diluted with 75 mL of CH_2Cl_2 and washed with three 100 mL portions of saturated $NaHCO_3$. The organic layer was then washed with brine, dried over Na_2SO_4 for 30 min, and rotavapped to yield a brown oil. The dark brown oil was then dissolved in minimal MeOH. Over the next 16 h, 0.398 g of the product precipitated as a white solid (28% yield). ^{1}H NMR (400 MHz, $CDCl_3$, 293 K): δ 6.95 (d, J = 2.8 Hz, 2H), 6.60 (d, J = 8.2, 2H), 6.54 (m, 2H), 3.71 (s, 4H), 3.27 (s, 4H), 2.82 (s, 4H), 1.43 (s, 18H), 0.98 (s, 18H), 0.96 (s, 18H), 0.16 (s, 12H), 0.15 (s, 12H). ^{13}C NMR (100 MHz, $CDCl_3$, 293 K): δ 171.02, 149.54, 147.82, 130.63, 121.06, 118.93, 118.35, 80.42, 55.77, 52.88, 52.78, 28.19, 25.92, 25.77, 18.28, 18.16, -4.13, -4.42. MS (ESI): Calcd for MH^+, 989.6322; Found, 989.6359. IR (cm^{-1}): 2950.62 (m), 2928.32 (m), 2894.88 (w), 2857.30 (m), 1719.16 (s), 1487.17 (s), 1470.49 (m), 1416.31 (w), 1390.24 (w), 1364.91 (m), 1288.47 (m), 1246.74 (s), 1200.42 (s), 1150.96 (m), 1125.18 (w), 1083.85 (w), 999.09 (w), 973.86 (m), 951.58 (w), 911.60 (s), 888.53 (m), 840.27 (s), 823.08 (s), 693.85 (m), 625.48 (w), 587.08 (m), 542.50 (w), 492.11 (w), 455.49 (w).

_N,N'_-Bis(2,5-dihydroxybenzyl)-_N,N'_-bis(_tert_-butyl-acetate)-1,2–ethanediamine (4).

_N,N'_-Bis[2,5-bis(_tert_-butyldimethylsiloxy)benzyl]-_N,N'_-bis(_tert_-butyl-acetate)-1,2–ethanediamine (536 mg, 0.542 mmol) was dissolved in 40 mL of tetrahydrofuran (THF) and

cooled to 0 °C. Acetic acid (0.50 mL, 8.7 mmol) and 2.71 mL of a 1.0 M solution of tetra-*N*-butylammonium fluoride (TBAF) in THF (2.71 mmol) were added. After the reaction mixture stirred for 3 h, 0.60 additional mL of the 1.0 M TBAF solution were added. The resultant solution stirred for another 2 h to ensure full removal of the *tert*-butyldimethylsilyl groups. 100 mL of water were added to quench the reaction, and the THF was removed by rotavaporation. The product was extracted from the aqueous solution with three 50 mL aliquots of CH_2Cl_2. The combined organic layers were washed with 150 mL of brine before being dried over Na_2SO_4 for 30 min. The crude was purified by column chromatography using 1:1 hexanes/EtOAc as the eluent (R_f = 0.25) to yield 222 mg of the product as a yellow oil (77% yield). We were unable to remove impurities that retained either one or two of the silane protecting groups. ^{1}H NMR (400 MHz, CD_3CN, 293 K): δ 9.06 (bs, 2H), 6.62 (m, 4H), 6.43 (d, J = 2.4, 2H), 6.40 (bs, 2H), 3.61 (s, 4H), 3.15 (s, 4H), 2.62 (s, 4H), 1.45 (s, 18H). ^{13}C NMR (100 MHz, CD_3CN, 293 K): δ 170.87, 150.24, 149.61, 122.83, 116.40, 116.23, 115.49, 81.41, 56.78, 55.50, 49.29, 27.32. Calcd for MH^+, 533.2863; Found, 533.2871. IR (cm^{-1}): 3211.89 (w), 2964.06 (m), 1726.78 (s), 1496.02 (s), 1366.96 (s), 1226.52 (s), 1148.54 (s), 983.99 (w), 893.64 (m), 816.58 (m), 776.75 (s), 735.93 (w), 597.05 (w).

_N,N'_-Bis(2,5-dihydroxybenzyl)ethanediamine-_N,N'_-diacetic acid (H_6qc1).

N,N'-Bis(2,5-dihydroxybenzyl)-*N,N'*-bis(*tert*-butyl-acetate)-1,2-ethanediamine (222 mg, 0.417 mmol) was dissolved in 10 mL of 90:5:5 trifluoroacetic acid/water/triisopropylsilane (TIS) and stirred for 24 h. The solvents were removed by rotavaporation. The product was washed with ether multiple times to remove the residual TIS and dried over air to yield 150 mg of the product as a white powder (86% yield). ^{1}H NMR (400 MHz, DMSO-d_6, 293 K): δ 8.83 (s, 2H), 6.62 (m, 6H), 3.93 (s, 4H), 3.60 (s, 4H), 3.14 (s, 4H). ^{13}C NMR (100 MHz, DMSO-d_6, 293 K): δ 170.87,

150.22, 149.20, 120.27, 118.56, 116.94, 116.51, 53.22, 52.84, 50.11. MS (ESI): Calcd for MH^+, 421.1611; Found, 421.1596. IR (cm^{-1}): 3043.9 (s), 1669.7 (s), 1513.11 (w), 1459.2 (m), 1435.4 (w), 1385.3 (m), 1365.6 (m), 1319.7 (w), 1261 (m), 1193.2 (s), 1131.2 (s), 1010.6 (w), 991.5 (w), 968.3 (w), 907.4 (w), 840.6 (m), 799.9 (m), 760.1 (m), 719.1 (m). UV/vis (50 HEPES buffered to pH 7.4): 294 nm (3500 M^{-1} cm^{-1}).

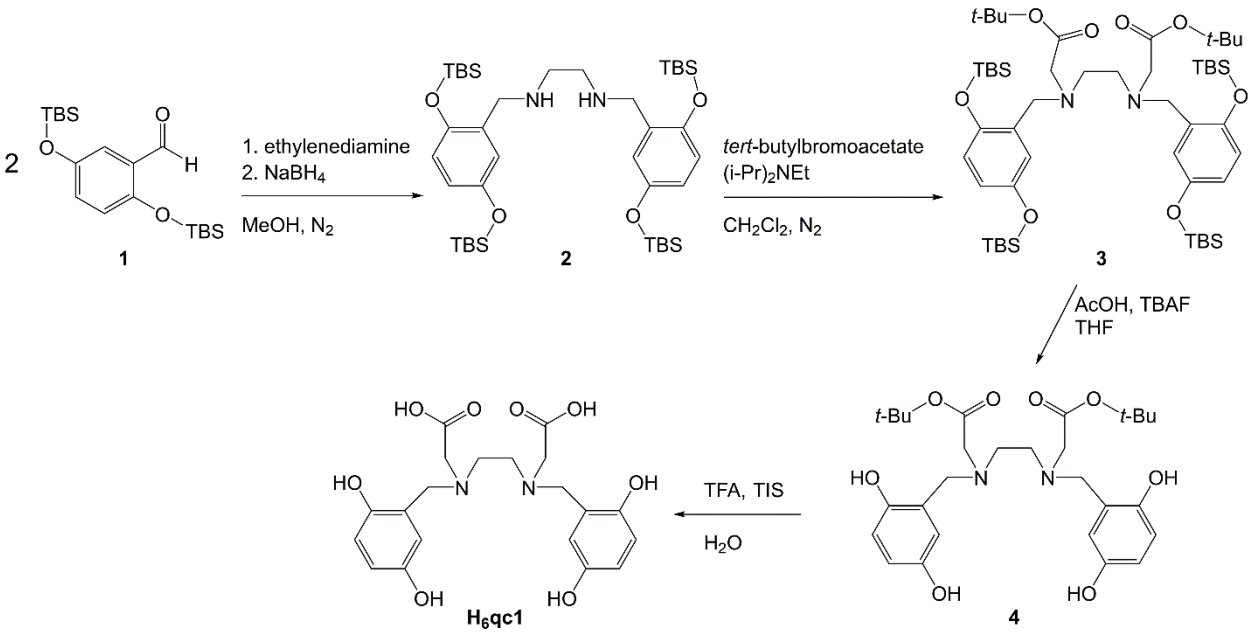

Scheme 3.3. Synthesis of H_6qc1

3.3 Results

Synthesis of H_6qc1

The ligand can be prepared in five steps from commercially available starting materials (Scheme 3.3); the first intermediate, 2,5-bis(*tert*-butyldimethylsiloxy)benzaldehyde (**1**), was previously synthesized by another research group.[20] The synthesis of H_6qc1 is more difficult than those used to prepare H_4qp2 and the related H_2qp1 (Scheme 3.2) for several reasons. First, two additional steps are required due to the need to protect both the quinols and the carboxylic acids. With H_2qp1 and H_4qp2, conversely, the quinols are added to the ligand framework late

enough in the synthesis to obliviate the need for their protection.[7, 8] Second, two of the intermediates need to be purified by column chromatography. H_2qp1 can be obtained in high purity without any chromatography;[7] whereas, H_4qp2 requires just a single column at the end of the synthesis.[8] Third, the addition of the protected carboxylic acids to yield **3** proved to be challenging. We eventually found that highly pure material would precipitate from MeOH, albeit in low yield (28%). Alternative means of purifying **3**, including column chromatography, did not effectively remove impurities. The immediate precursor to H_6qc1, **4**, could not be obtained in high purity, but the impurities were removed in the final step of the synthesis, as confirmed by NMR.

We attempted to isolate a Mn(II) complex with H_6qc1 but were unable to precipitate clean material from a variety of solvents, including water, MeCN, CH_2Cl_2, and MeOH. Given this, studies on the Mn(II) were done on samples prepared *in situ*; this has been done with other manganese-containing complexes, including some MRI contrast agents.[11-13]

Aqueous Characterization of the H_6qc1 Ligand

We analyzed the behavior of the H_6qc1 ligand by itself in an aqueous solution containing 100 mM KCl via potentiometric pH titrations. Our best fitting model for the titration data displays five ionization events as the pH increased from 2 to 10.5 (Table 1, Figure S3.19). We did not collect or model data past pH 10.5, as was done with HBED,[13, 14] since the ligand displays irreversible degradation under those conditions. Using the speciation of HBED as a model, the H_6qc1 ligand likely exists as $[H_8qc1]^{2+}$ under extremely acidic conditions, with two protons localized on each of the amines.[14] The first three ionization events correspond to pK_a values of 2.45 (±0.3), 2.89 (±0.05), and 4.31 (±0.05). These likely correspond to the deprotonation of the first ammonium and the two carboxylic acids and the formation of H_7qc1^+,

H_6qc1, and H_5qc1^-. The amine and the carboxylate conjugate bases are anticipated to accept intramolecular hydrogen bonds from the remaining ammonium and the two quinols, as was seen in the crystal structure of the free H_2qp1 ligand.[21] The other two pK_a values resulting from the model are 8.80 (±0.05) and 11.67 (±0.3); the associated deprotonation reaction would yield H_4qc1^{2-} and H_3qc1^{3-}. The error in the 11.67 pK_a is larger since we could not fully generate the species during the titrations. The HBED ligand has similar pK_a values of 1.7, 2.53, 4.72, 8.44, and 11.00, plus another at 12.60.[14] The UV/vis spectrum of H_6qc1 in water changes substantially as the pH increases from 7.4 to 9.0 (Figure S3.21). At low pH values, there is a strong feature at 299 nm, which is consistent with a phenol or quinol group.[8, 10] As the solution becomes more basic, however, a lower-energy band at 330 nm develops; the energy of this feature is more consistent with a phenolate or quinolate group. The proton that is lost from the ligand as the pH increases from 7.4 to 9.0 appears to be at least partially localized on the quinol. Between pH 7.0 and 7.4, the H_6qc1 ligand therefore predominantly exists as H_5qc1^-, with a trace amount of H_4qc1^{2-} (Figure 3.1).

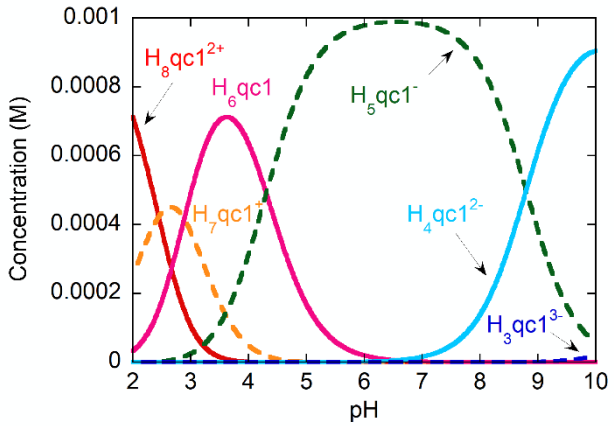

Figure 3.1. Predicted speciation as a function of pH for 1.0 mM H_6qc1 in 100 mM KCl solution.

Table 3.1. pMn and pK_a Values for the Ligands and Mn(II) Complexes with H_6qc1 Determined by Potentiometric Titration at 25 °C.

pK_{L1}[a]	11.670 (±0.3)	pK_{a1}[b]	8.02 (±0.06)
pK_{L2}[a]	8.80 (±0.05)	pK_{a2}[b]	6.19 (±0.06)
pK_{L3}[a]	4.31 (±0.05)	pK_{a3}[b]	4.24 (±0.06)
pK_{L4}[a]	2.89 (±0.05)	log K(MnH_3qc1)[c]	15.59
pK_{L5}[a]	2.45 (±0.3)	log K(MnH_4qc1)[c]	10.11
		log K(MnH_5qc1)[c]	5.55
		pMn (pH 7.4)[d]	6.67

[a]Ligand pK_a values correspond to the following equilibrium constants: $K_{L1} = [(H_3qc1)^-][H^+]/[(H_4qc1)^{2-}]$, $pK_{L1} = \log\beta_{110} - \log\beta_{010}$; $K_{L2} = [(H_4qc1)^{2-}][H^+]/[(H_5qc1)^-]$, $pK_{L2} = \log\beta_{210} - \log\beta_{110}$; $K_{L3} = [(H_5qc1)^-][H^+]/[(H_6qc1)]$, $pK_{L3} = \log\beta_{310} - \log\beta_{210}$; $K_{L4} = [(H_6qc1)][H^+]/[(H_7qc1)^+]$, $pK_{L4} = \log\beta_{410} - \log\beta_{310;}$ $K_{L5} = [(H_7qc1)^+][H^+]/[(H_8qc1)^{2+}]$, $pK_{L5} = \log\beta_{510} - \log\beta_{410}$.

[b]Metal complex pK_a values correspond to the following equilibrium constants: $K_{a1} = [[Mn(H_2qc1)]^{2-}][H^+]/[[Mn(H_3qc1)]^-]$, $pK_{a1} = \log\beta_{011} - \log\beta_{-111}$; $K_{a2} = [[Mn(H_3qc1)]^-][H^+]/[[Mn(H_4qc1)]]$, $pK_{a12} = \log\beta_{111} - \log\beta_{011}$.; $K_{a3} = [[Mn(H_4qc1)]][H^+]/[[Mn(H_5qc1)^+]]$, $pK_{a13} = \log\beta_{211} - \log\beta_{111}$.

[c]Metal complex stability constants correspond to the following equilibrium constants: $K(MnH_3qc1) = [[Mn(H_3qc1)^-]]/[Mn^{2+}][H_3qc1^{3-}]$; $K(MnH_4qc1) = [[Mn(H_4qc1)]]/[Mn^{2+}][H_4qc1^{2-}]$; $K(MnH_5qc1) = [[Mn(H_5qc1)^+]]/[Mn^{2+}][H_5qc1^-]$

[d]log(free Mn(II)) at pH 7.4 with 1.0 mM Mn(II) and 1.0 mM H_6qc1.

Aqueous Characterization of the Mn(II) Complex with H_6qc1

The speciation of Mn(II) complexes with H_6qc1 in water was analyzed using a 100 mM solution of KCl containing a 1:1 mixture of $MnCl_2$ and ligand. The curves resulting from the potentiometric pH titrations (Figure S3.22) look distinct from those for the metal-free H_6qc1, and only four clear ionization events are observed as the pH is increased from 2.6 to 10.2. As with our analysis of the titration data for free H_6qc1, the inclusion of additional species into the model worsened the fit (Figure S3.23). The first ionization event corresponds to the release of Mn(II) from the ligand. The next three ionization events are assigned to (de)protonation events for the H_6qc1-Mn(II) complex and are correspond to pK_a values of 4.24 (±0.06), 6.19 (±0.06), and 8.02 (±0.06) (Table 3.1). The UV/vis bands of an aqueous 1:1 mixture of $MnCl_2$ and H_6qc1 change

substantially from pH 5 to 9 (Figure S3.24), leading us to assign the 6.19 and 8.02 pK_a values to the deprotonation of the Mn(II)-bound quinols.[8] The acid/base behavior is similar to the Mn(II)-HBED system, which has pK_a values of 6.58 and 7.66 for the deprotonation of Mn(II)-bound phenols.[13]

The speciation of the Mn(II) as a function of pH is shown in Figure 2. Our model of the data suggests that the Mn(II)-H_6qc1 complex is indeed more stable than Mn(II)-H_4qp2 but is less stable than Mn(II)-H_2qp1 The pMn value at pH 7.4, 1.0 mM total Mn(II), and 1.0 mM total ligand is 6.67; the pMn values for the H_2qp1 and H_4qp2 systems under identical conditions, conversely, were found to be 7.25 and 5.36, respectively.[8, 22] At pH 7, the Mn(II) exists predominantly as $[Mn(H_3qc1)]^-$, with a substantial amount of $[Mn(H_2qc1)]^{2-}$. Since we could not assess the stability of the fully deprotonated ligand, H_2qc1^{4-}, we were unable to measure a K_{eq} value for the complexation of the tetraanionic ligand with Mn(II), but we were able to measure values for the Mn(II) complexes with H_5qc1^-, H_4qc1^{2-}, and H_3qc1^{3-} (Table 3.1). These values demonstrate that the H_6qc1 species are substantially more stable than their HBED analogs; the log K values for the Mn(II) complexes with the doubly and triply deprotonated ligands are 5.56 and 9.98 respectively.[13]

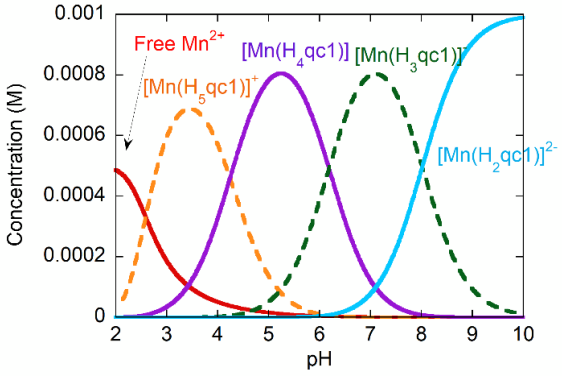

Figure 3.2. Predicted speciation of Mn(II) as a function of pH for an aqueous solution containing 1.0 mM $MnCl_2$, 1.0 mM H_6qc1, and 100 mM KCl.

Oxidative Stability of the H_6qc1 Ligand and its Mn(II) Complex

Neither the ligand nor its Mn(II) complex appears to react with O_2 in aqueous solution over several hours as assessed by UV/vis analysis of solutions of these compounds exposed to air (Figures S3.25 and S3.26). The UV/vis spectrum of each compound remains approximately the same. The stability of the Mn(II) complex to air was also confirmed by EPR (Figure S3.27). Although the H_6qc1 ligand by itself does not react with H_2O_2 over the course of 1 h (Figure S3.28), its Mn(II) complex reacts quickly with this oxidant as assessed by both UV/vis and EPR. In 50 mM HEPES buffered to pH 7.0, the Mn(II) complex initially displays three bands at 298 nm, 368 nm, and 481 nm (Figure 3.3). Upon the addition of H_2O_2, all three peaks increase in intensity over the course of 5 min but then weaken. The band at 298 nm eventually disappears completely, suggesting that the quinols have been oxidized. Over the course of 1 h, a broad band centered at 482 nm steadily develops. UV/vis peaks with similar energies have been previously observed for Mn(III) species.[23, 24] Parallel reactions analyzed by EPR confirm that the metal is being oxidized to an EPR-silent species, with the Mn(II) signal steadily vanishing over 30 min (Figure 3.4). We are currently unable to separate these oxidized manganese products and have therefore been unable to obtain stability measurements for any of the individual species.

We were unable to obtain clean samples of the demetallated and oxidized form(s) of the ligand. We instead analyzed the ligand oxidation by adding $Zn(OTf)_2$ to reactions containing 1:1 mixtures of H_6qc1 and $MnCl_2$ with or without H_2O_2. The Zn(II) displaces the manganese from the ligand, yielding species that can be readily visualized by ^{1}H NMR. The addition of H_2O_2 decreases the intensity of the aromatic peaks relative to the benzylic ones; this is consistent with the loss of the OH protons and the oxidation of the quinols to *para*-quinones (Figure S3.29).[7, 8]

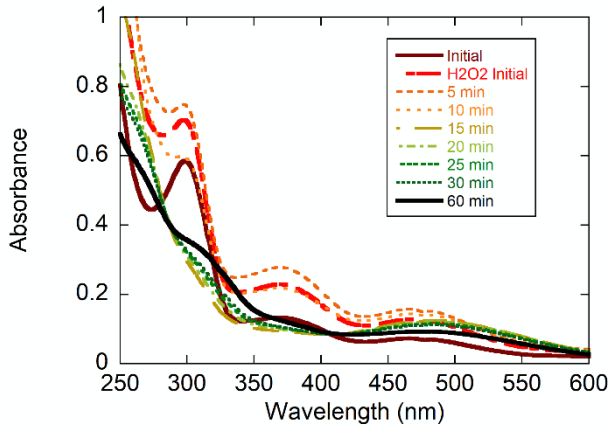

Figure 3.3. Spectrophotometric response of an aqueous solution containing 0.1 mM $MnCl_2$, 0.1 mM H_6qc1, and 50 mM HEPES buffered to pH 7.0 to 43 mM H_2O_2.

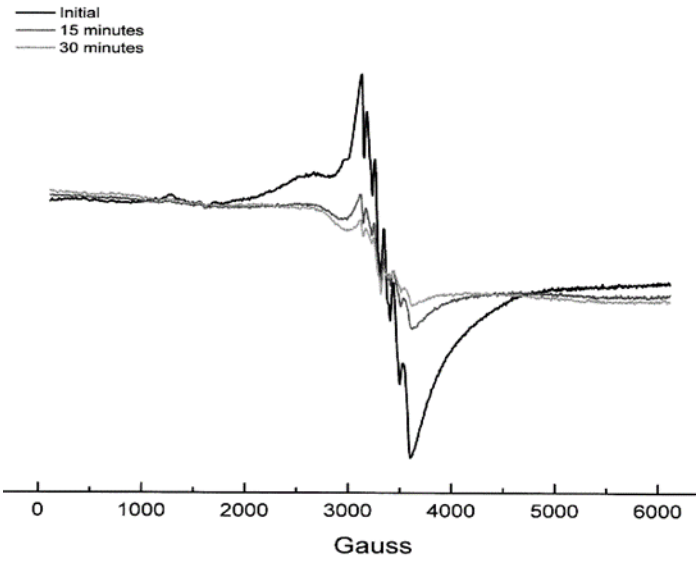

Figure 3.4. EPR spectra showing the oxidation of an aqueous 1:1 mixture of $MnCl_2$ and H_6qc1 by H_2O_2 over 30 min. All solutions contained 1.0 mM $MnCl_2$, 1.0 mM H_6qc1, and 50 mM HEPES buffered to pH 7.0. 10 mM of H_2O_2 was added, and the reaction was allowed to proceed at RT. Aliquots were removed and frozen for EPR analysis at 15 min and 30 min.

Measurement of T1-Weighted Relaxivity for the Mn(II) and its Oxidized Products

The Mn(II) complex with H_6qc1 displays distinct spectroscopic changes upon reaction with H_2O_2, but not O_2, prompting us to investigate whether the compound could selectively

detect H_2O_2 via changes in its *T1*-weighted relaxivity (*r1*). We characterized the reaction between H_2O_2 and the Mn(II)-H_6qc1 complex using methodology that we had developed for prior H_2O_2 sensors.[6-8] We measured the *T1* values of 1:1 mixtures of $MnCl_2$ and H_6qc1 in aqueous solutions buffered to pH 7.0 using a 3T MRI scanner. The concentration of Mn(II) was varied from 0.10 mM to 1.0 mM, and the slope of (1/*T1*) versus the concentration provides *r1*. A second set of solutions contained 10 mM H_2O_2 in order to oxidize the Mn(II)-H_6qc1 complex; these were allowed to react for 30 min in order to ensure that the reactions went to completion. Unexpectedly, the presence of H_2O_2 neither increased nor decreased the *r1* of the manganese/H_6qc1 mixtures. In phosphate buffer, the *r1* values before and after adding H_2O_2, 3.48 and 3.46 mM^{-1} s^{-1}, are within error of each other (Figure 3.5). A significant response to H_2O_2 was likewise absent when the complex was studied in 50 mM HEPES buffered to pH 7.0. In one instance, we observed a 10% increase in *r1* (Figure S3.30), but this was not reproducible.

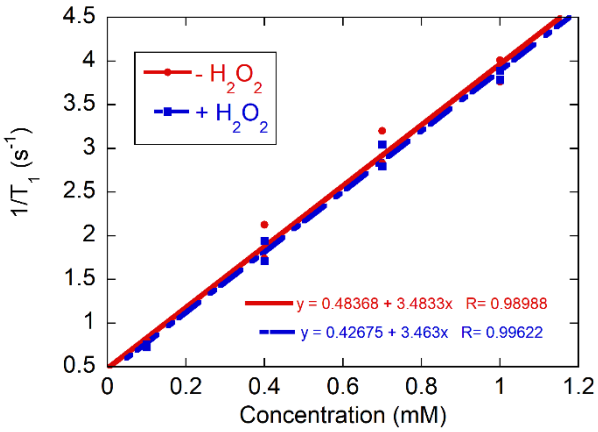

Figure 3.5. *T1*-weighted relaxivity (*r1*) data for 1:1 mixtures of $MnCl_2$ and H_6qc1 in the absence and presence of excess (10 mM) H_2O_2 in an aqueous solution containing 50 mM Na_3PO_4 buffered to pH 7.00. All samples were analyzed at 298 K with a 3 T clinical MRI scanner. All samples were prepared under air and run within 30 min of preparation.

3.4 Discussion

Redox-active ligands have found increasing use within many subfields of inorganic chemistry.[25-31] Our own interest in this area has centered on using quinol-containing molecules to prepare complexes that display oxidation-triggered increases in their *T1*-weighted relaxivity (*r1*) and/or catalyze the degradation of superoxide.[7, 8, 21] Both applications rely upon the quinols within the organic ligands reversibly oxidizing to *para*-quinones (Scheme 1). The first two polydentate ligands, H_2qp1 and H_4qp2 (Scheme 3.2), use amines and pyridines as the other chelating groups. Although their complexes with Zn(II) thus far appear to be highly stable in water,[21] these neutral N-donors bind much more weakly to Mn(II).[8] As a consequence, the H_4qp2 complex with Mn(II) is just barely stable enough to function at pH 7, and its oxidation to di-*para*-quinone (qp2) and mono-*para*-quinone forms (H_2qp2) appear release substantial amounts of Mn(II).

In order to prepare a ligand that can more tightly coordinate Mn(II), we have replaced the pyridines of H_4qp2 with carboxylic acids to yield H_6qc1 (Scheme 3.2). Although the ligand is much more challenging to synthesize than H_4qp2, the changes to the molecule do improve its affinity for Mn(II). The pMn value for H_6qc1 (pH 7.4, 1.0 mM total Mn(II), 1.0 mM total ligand) is 6.67, which is over an order of magnitude improvement over the 5.36 value reported for the H_4qp2 system but is worse than the 7.25 value measured for H_2qp1.[8, 22] Substantial metal dissociation is still observed under highly acidic conditions (Figure 3.2). The superior binding affinity of H_2qp1 for Mn(II) is initially difficult to rationalize, since the latter ligand cannot attain as negative a charge. The quinol portions of the ligands, however, appear to bind to metal ions poorly in their neutral forms, and they are often detached from the metal ions in crystal structures.[8, 21] Under neutral to acidic conditions, H_2qp1 consistently provides five

strong donor atoms as opposed to the four from H_6qc1. We believe that the extra effective donor atom of H_2qp1 more than compensates for its less negative charge, particularly under acidic conditions.

Unexpectedly, the quinols appear to bind to the Mn(II) much more tightly than phenols, for the stability constants of the [Mn(H_3qc1)]$^-$ and [Mn(H_4qc1)] complexes (Table 3.1) are higher than those for their analogs with the related HBED ligand, which contains phenols instead of quinols (Scheme 3.2).[13] This appears to be a reproducible effect since the Mn(II) complex with H_2qp1 is substantially more stable than the Mn(II) complex with Hptp1 (Scheme 3.4), which has a pMn of 5.40 at pH 7.4.[15]

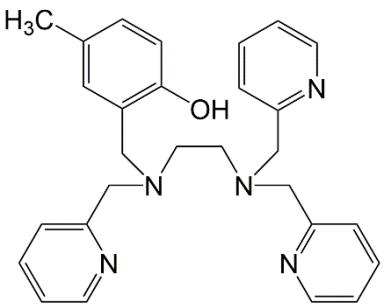

Hptp1

Scheme 3.4

The more anionic charge of the H_6qc1 ligand has a weak impact on the interaction between the quinols and the metal center. The Mn(II) complexes with H_6qc1 and H_4qp2 have similar pK_a values for their Mn(II)-quinol groups: 6.19 and 8.02 for H_6qc1 versus 5.82 and 7.14 for H_4qp2.[8] The acid/base behavior of the Mn(II) complex strongly resembles that observed for its analog with HBED, which has pK_a values of 6.58 and 7.66.[13]

Highly anionic ligands, such as ethylenediaminetetraacetate (EDTA^{4-}), often stabilize Mn(III) species,[32] and the more negatively charged coordination sphere provided by H_6qc1

around pH 7 does render the metal center more susceptible to oxidation. Neither the H_4qp2 nor the H_6qc1 complex with Mn(II) displays any substantial spectroscopic change upon a 4 h reaction with air. [Mn(H_4qp2)Br_2] is slowly oxidized a Mn(III) species upon reaction with H_2O_2, but this is not noticeable by EPR at 30 min.[8] The Mn(II) complex with H_6qc1, conversely, quickly reacts with H_2O_2 to yield what we believe are one or more Mn(III)-containing products, as assessed by both UV/vis and EPR (Figure 3.3, Figure 3.4). Oxidation to Mn(IV) is unlikely since new signals do not appear in the EPR spectrum. The ligand appears to be oxidized as well, as evidenced by both UV/vis and ^{1}H NMR (Figure 3.3, Figure S3.29). We have thus far been unable to isolate any individual manganese-containing products from these reaction mixtures.

It is challenging to predict the overall impact of H_2O_2 on the *T1*-weighted relaxivity of the manganese complex with H_6qc1 since both the ligand and metal are being oxidized during the reaction. The Mn(II) sensors with H_2qp1 and H_4qp2 react with H_2O_2 to yield Mn(II) species with higher *r1* values, which we attributed to water molecules displacing the *para*-quinone groups of the oxidized ligands (Scheme 3.1).[7, 8] More highly aquated metal centers tend to have higher *r1* values. The oxidation of the metal center by H_2O_2, conversely, would be anticipated to worsen the *r1* since the metal ion would be rendered less paramagnetic by this process.[10, 33] Another factor that impacts *r1* is the rate of water exchange. Oxidation to Mn(III) would be anticipated to slow the rate of exchange,[34] but the value that would optimize *r1* has not yet been established for either Mn(II) or Mn(III) complexes. Unexpectedly, the oxidation of 1:1 Mn(II)/H_6qc1 mixtures by H_2O_2 results in no observable change to the *r1* at pH 7.0 (Figure 3.5). The relaxivity is impacted by the choice of buffer; the Mn(II)-H_6qc1 complex is more effective in 50 mM HEPES solution (3.98 mM^{-1} s^{-1}) than in 50 mM phosphate (3.48 mM^{-1} s^{-1}). Phosphate is known to compete with superoxide in manganese-containing superoxide

dismutase mimics,[15, 35, 36] and this may decrease *r1* by competing with water for vacant coordination sites on the metal ion. In one set of experiments, we observed a 10% increase in *r1* in HEPES solution upon adding H_2O_2 (Figure S3.30), which is much smaller than the 30% increase we observed for the H_4qp2 system,[8] but we could not replicate this in other experiments. Determining the impact of aquation on *r1* is complicated by the lack of a protocol for measuring solution state aquation numbers for Mn(III) species.

3.5 Conclusion

The substitution of two carboxylate groups for the pyridines in the H_4qp2 ligand allows the resultant H_6qc1 ligand to bind more tightly to Mn(II). Unfortunately, the more anionic coordination sphere facilitates oxidation of the metal center, which in turn, eliminates the H_2O_2-triggered increase in *T1*-weighted relaxivity that was observed for the related H_4qp2 probe. Although the new ligand is unsuitable for manganese-containing MRI contrast agent sensors for H_2O_2, the presence of redox-active functionalities and its strongly anionic charge may make this ligand useful for other applications.

Appendix 2

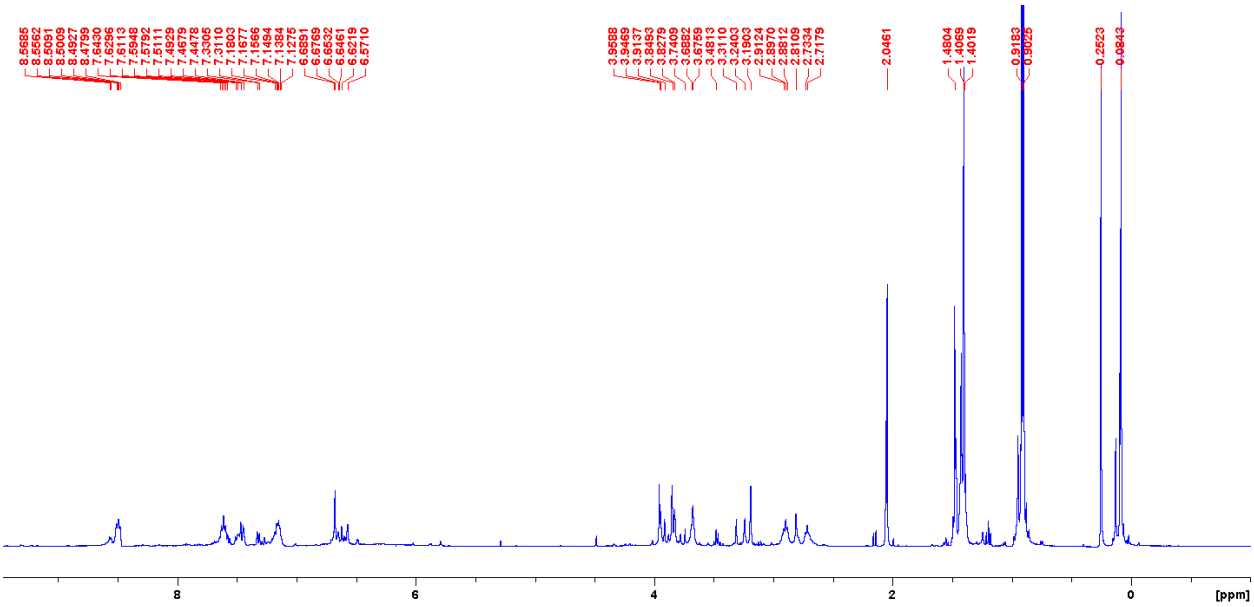

Figure S3.1: ^{1}H NMR of **3** in $CDCl_3$.

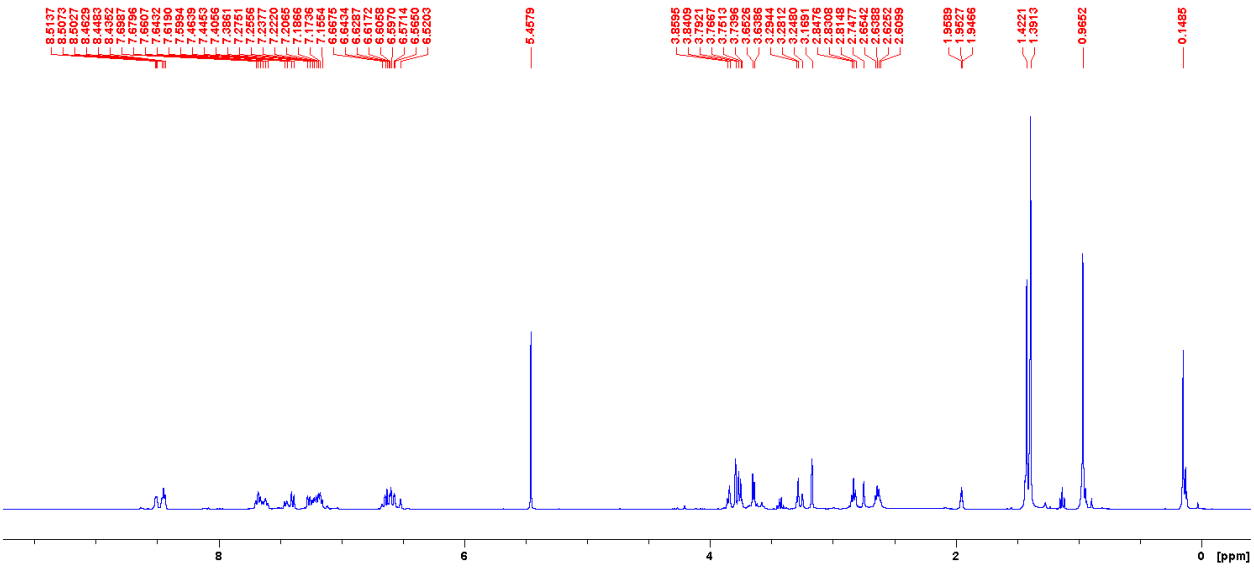

Figure S3.2: ^{1}H NMR of **4** in $CDCl_3$.

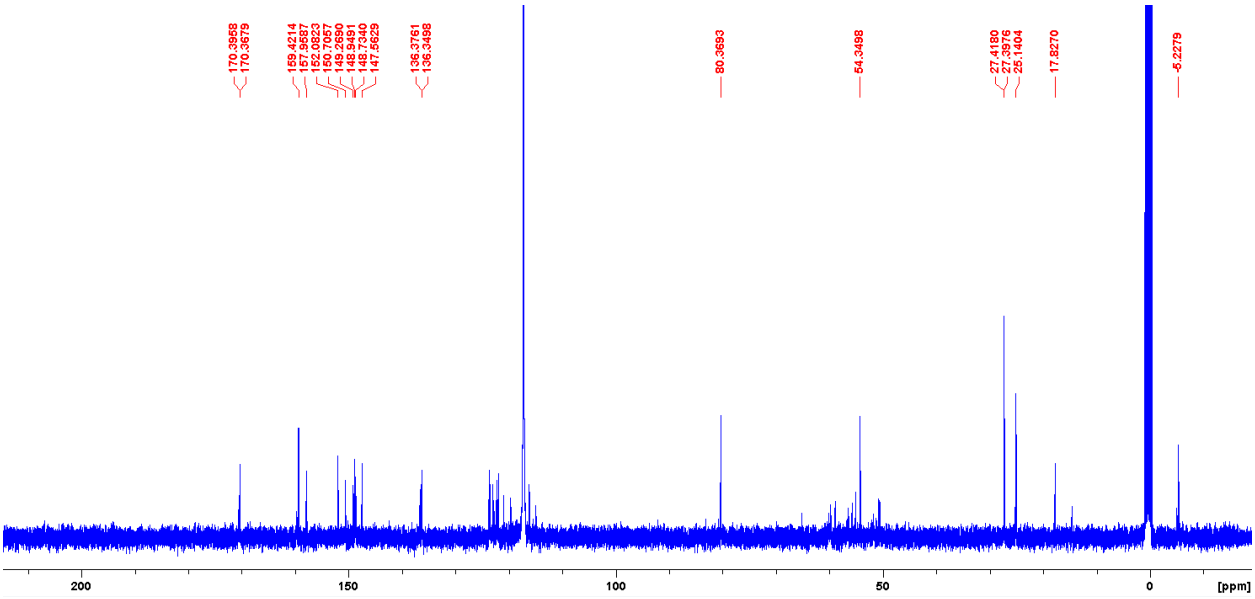

Figure S3.3: ^{13}C NMR of **4** in $CDCl_3$.

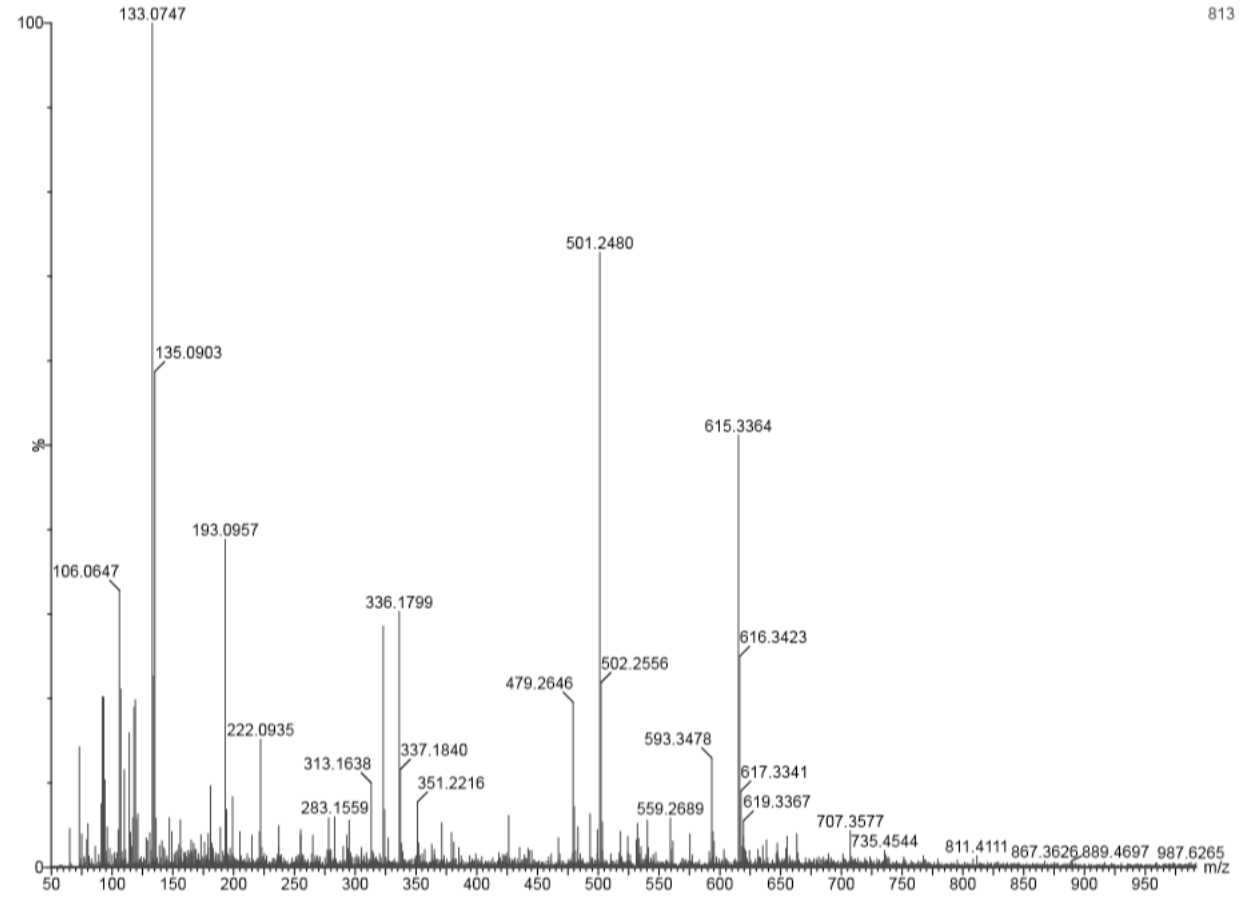

Figure S3.4: MS of product **4** in $CDCl_3$.

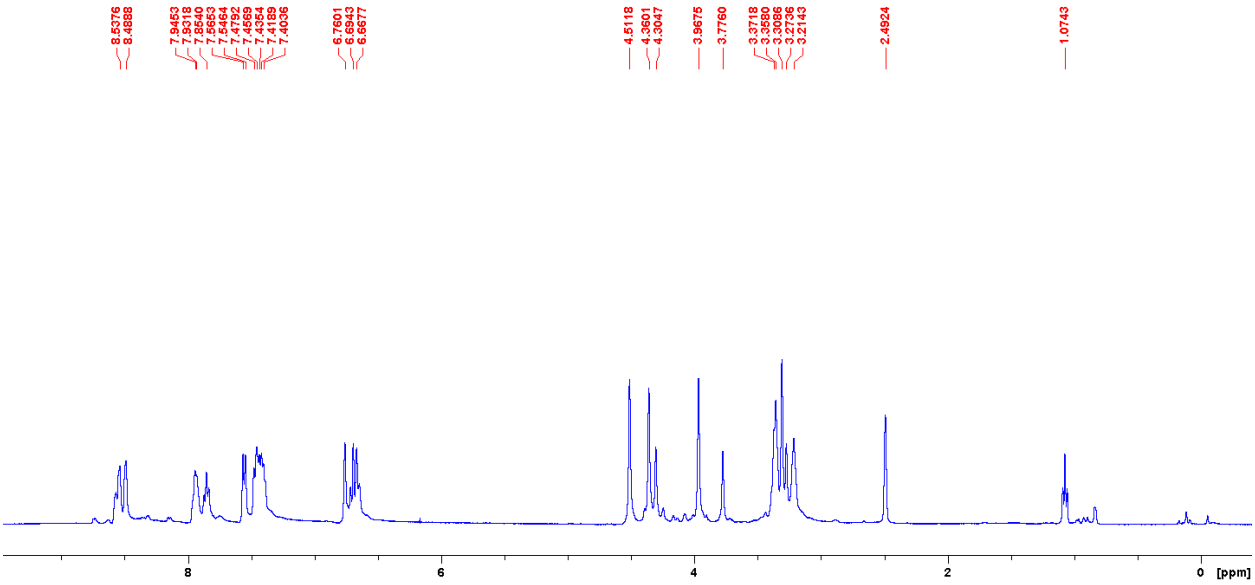

Figure S3.4: ^{1}H NMR of **5** in $CDCl_3$.

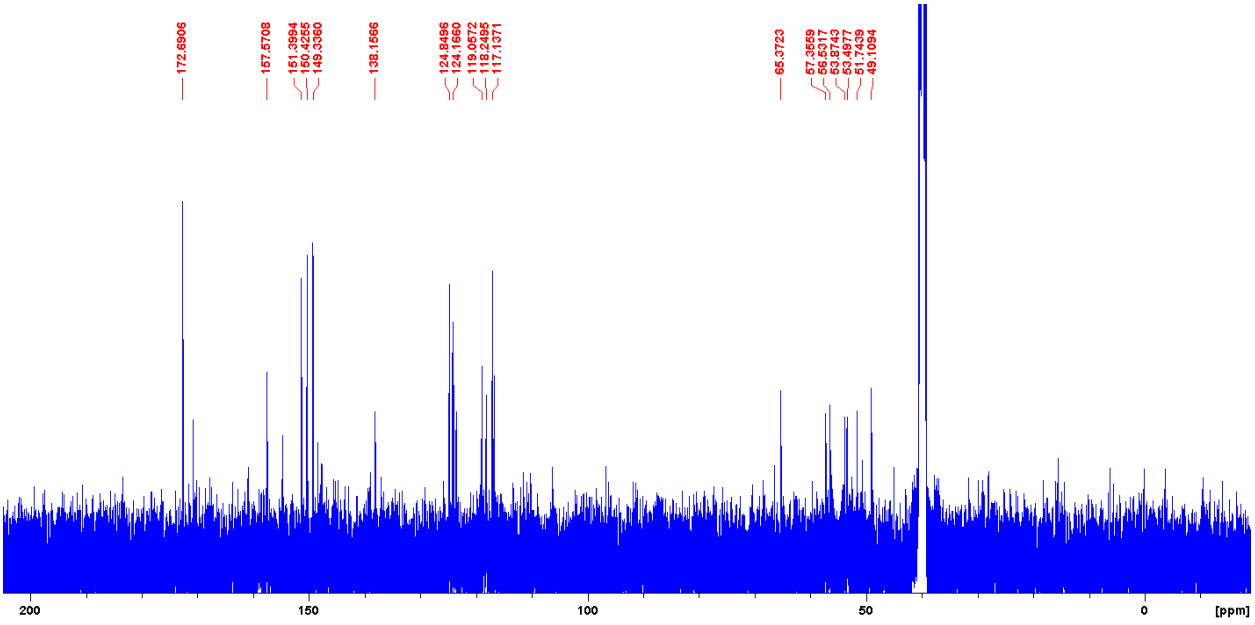

Figure S3.5: ^{13}C NMR of **5** in $CDCl_3$.

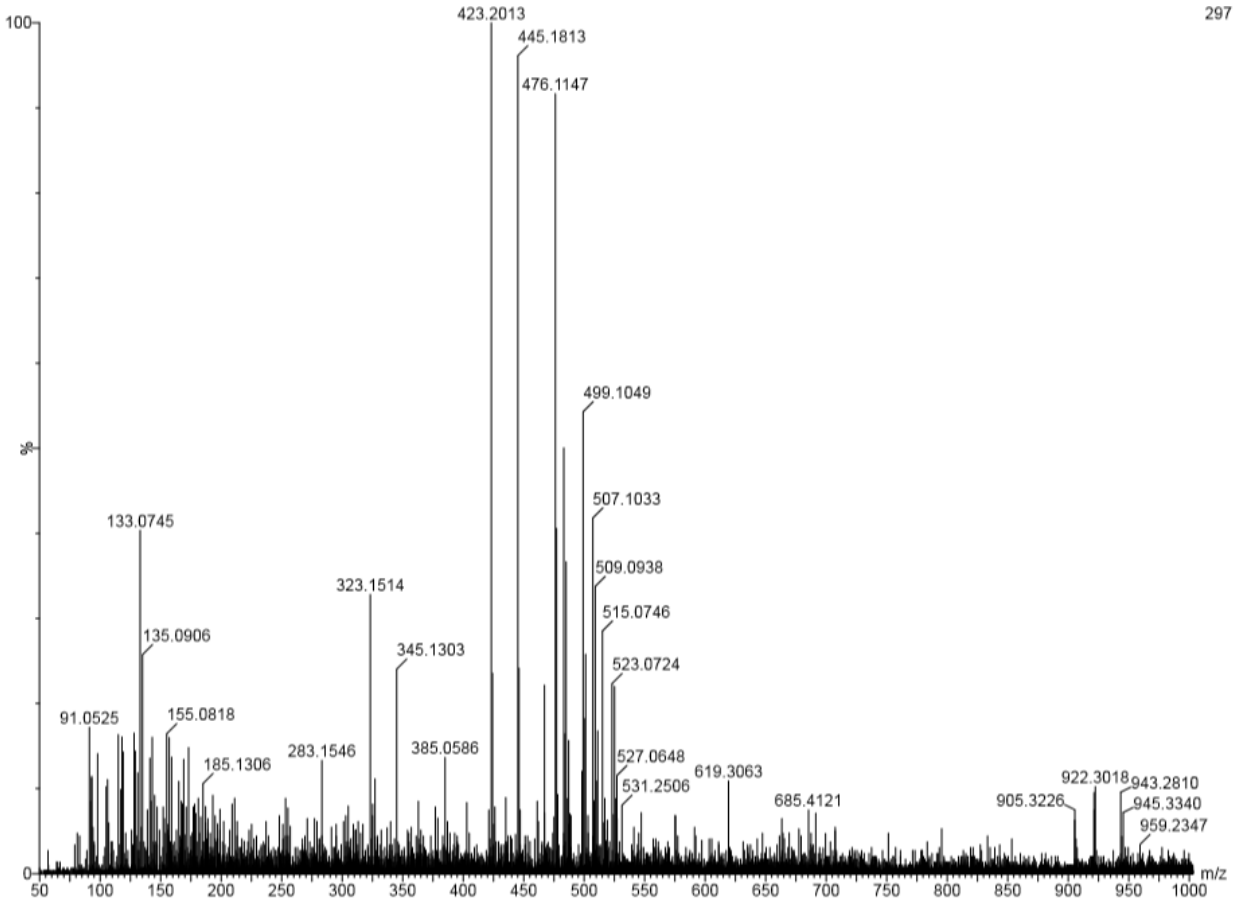

Figure S3.6: MS of product **5** in $CDCl_3$.

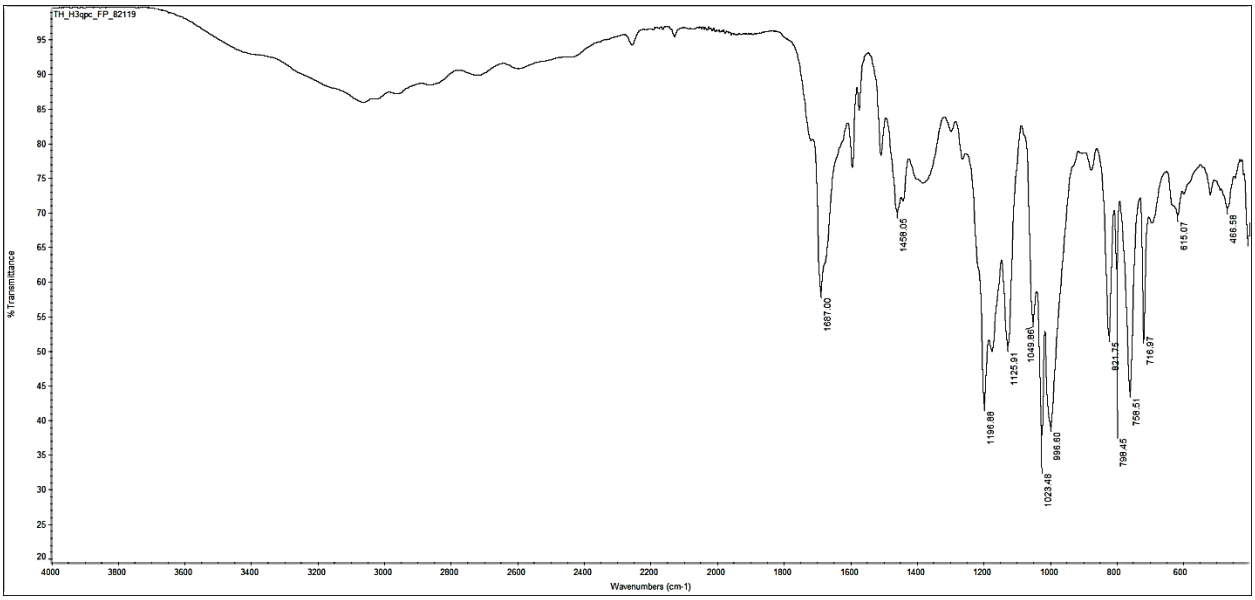

Figure S3.7: IR of Product **5**.

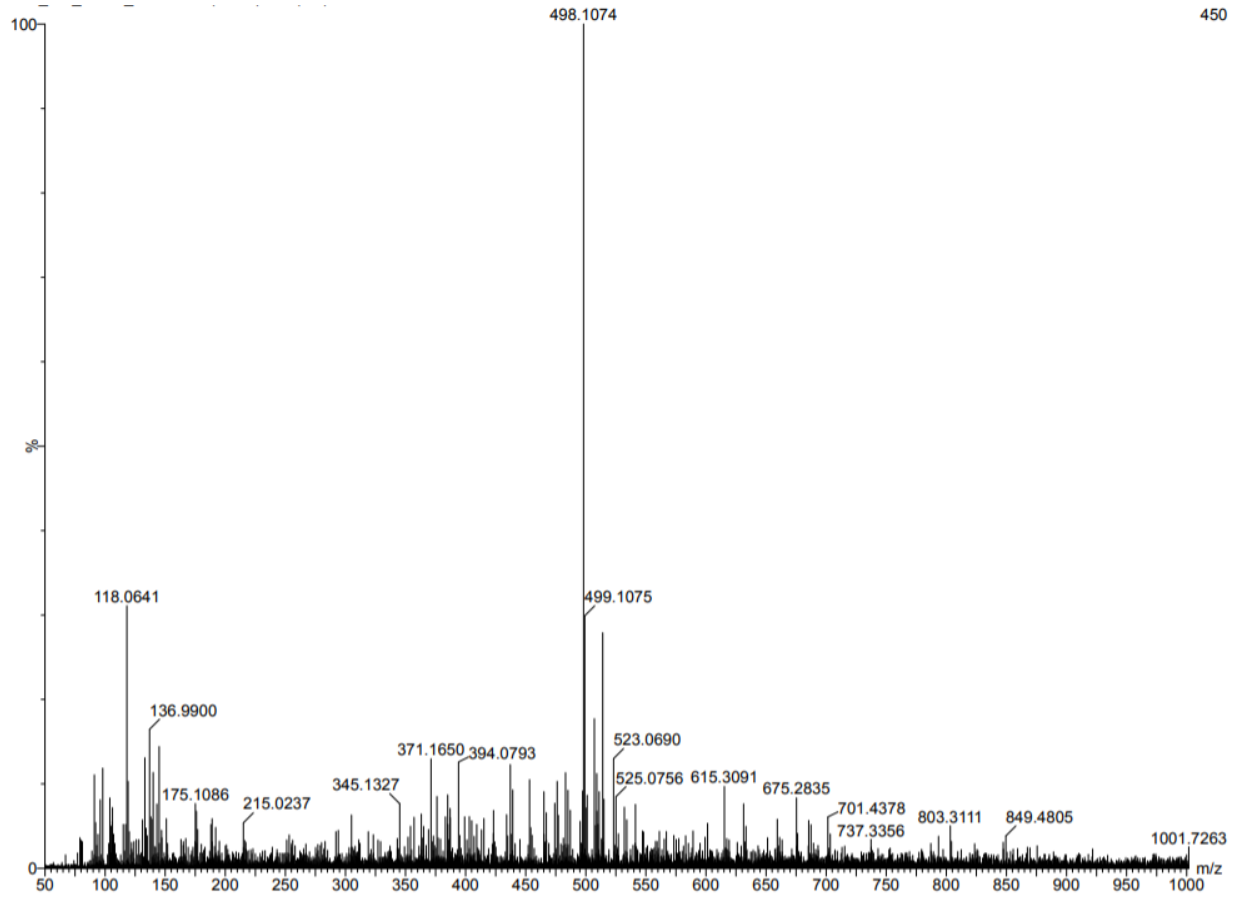

Figure S3.8: MS of Mn(II)H_3qpc in MeCN.

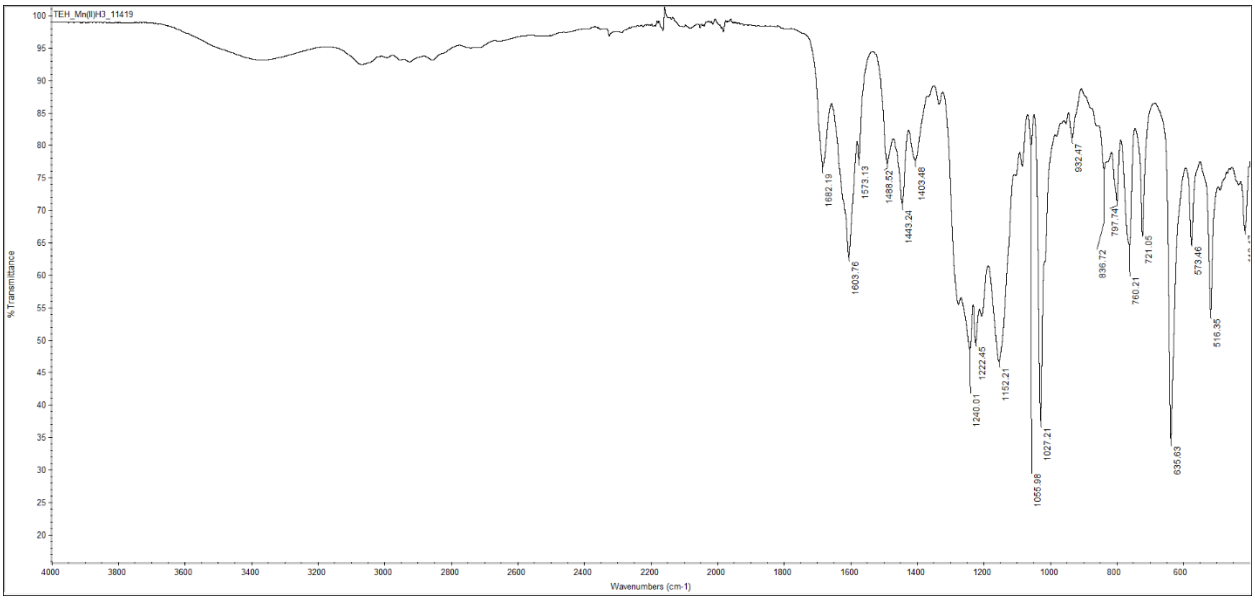

Figure S3.9: IR of Mn(II)H_3qpc.

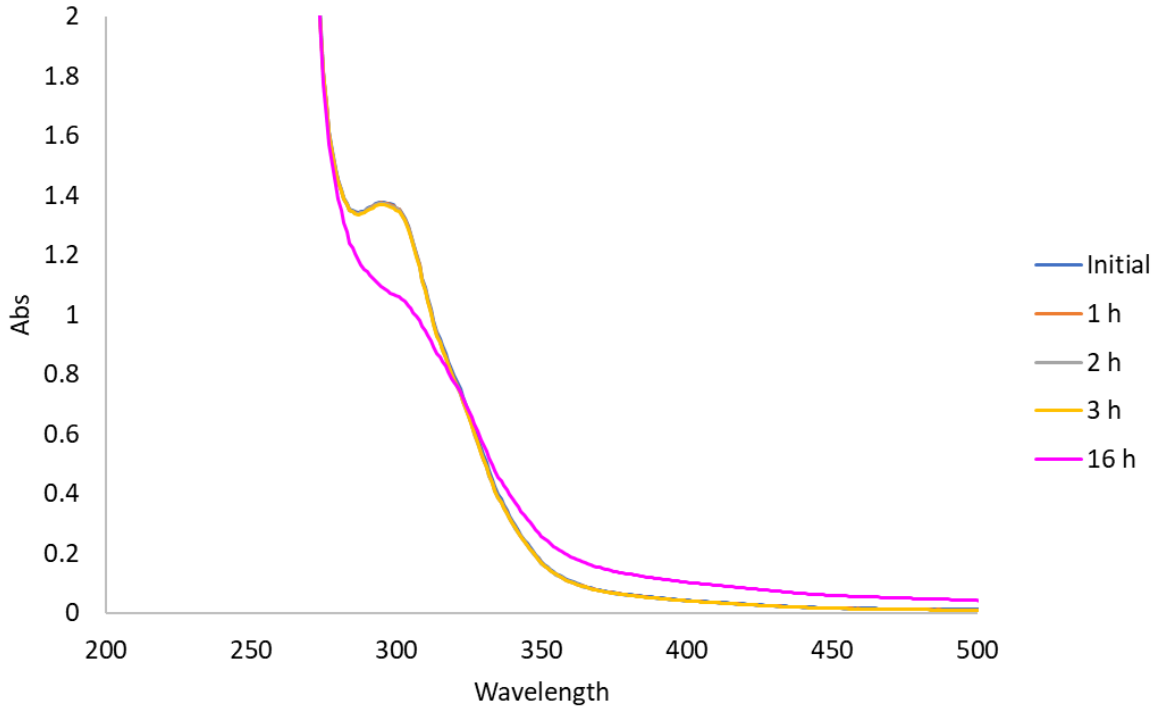

Figure S3.10: UV-VIS of Mn(II)H3qpc 0.1 M in MeCN under N_2.

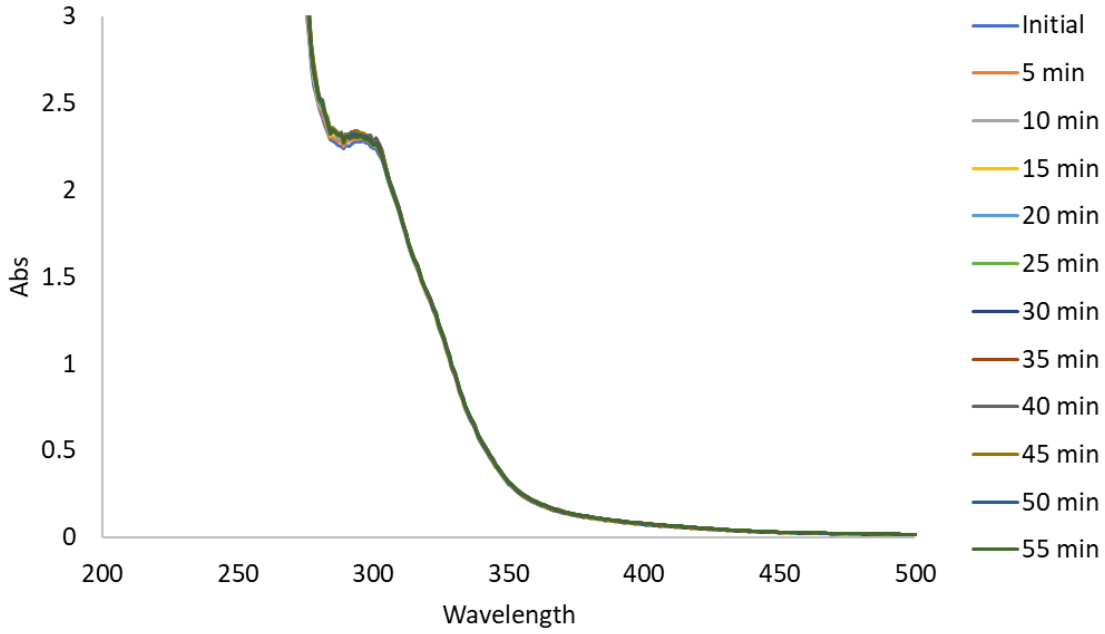

Figure S3.11: UV-VIS of Mn(II)H_3qpc 0.1 M in MeCN open to air.

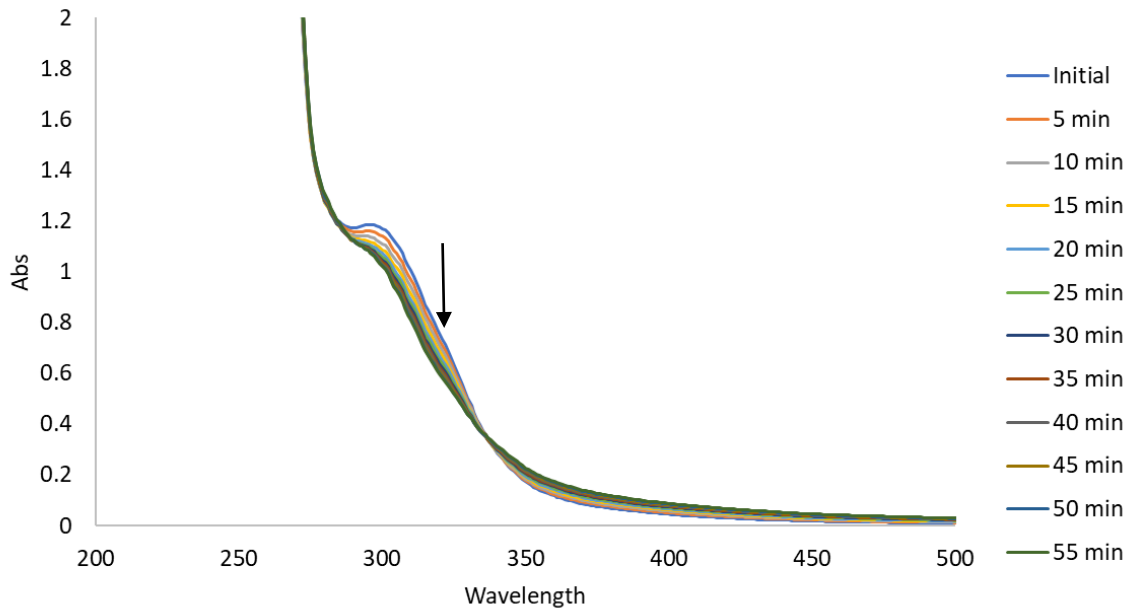

Figure S3.12: UV-VIS of Mn(II)H_3qpc 0.1 M in MeCN with 10 eq. of 10 mM H_2O_2.

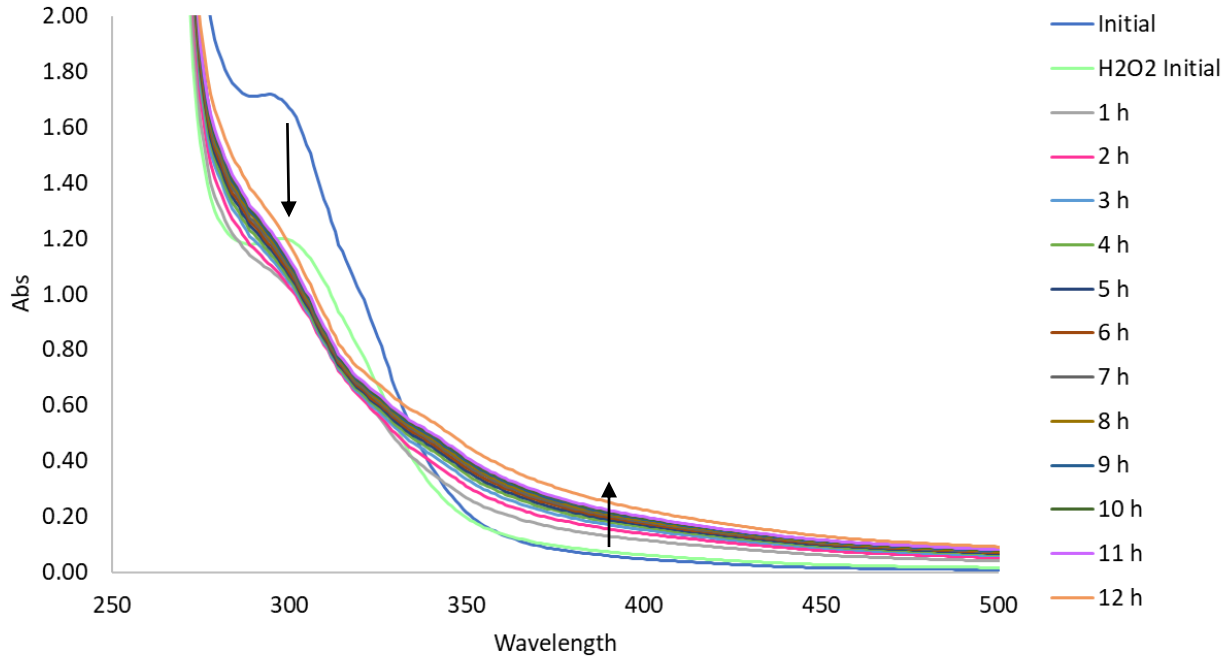

Figure S3.13: UV-VIS of Mn(II)H_3qpc 0.1 M in MeCN with 10 eq. of 10 mM H_2O_2.

References

1. L. Tretter, I. Sipos, V. Adam-Vizi, *Neurochem. Res*., **29** (2004) 569-577.
2. C.K. Roberts, K.K. Sindhu, *Life Sci.*, **84** (2009) 705-712.
3. R.L. Mosley, E.J. Benner, I. Kadiu, M. Thomas, M.D. Boska, K. Hasan, C. Laurie, H.E. Gendelman, *Clin. Neurosci. Res*., **6** (2006) 261-281.
4. I.M. Fearon, S.P. Faux, *J. Mol. Cell. Cardiol*., **47** (2009) 372-381.
5. G. Eskici, P.H. Axelsen, *Biochemistry*, **51** (2012) 6289-6311.
6. M. Yu, R.J. Beyers, J.D. Gorden, J.N. Cross, C.R. Goldsmith, *Inorg. Chem*., **51** (2012) 9153-9155.
7. M. Yu, S.L. Ambrose, Z.L. Whaley, S. Fan, J.D. Gorden, R.J. Beyers, D.D. Schwartz, C.R. Goldsmith, *J. Am. Chem. Soc*., **136** (2014) 12836-12839.
8. M. Yu, M.B. Ward, A. Franke, S.L. Ambrose, Z.L. Whaley, T.M. Bradford, J.D. Gorden, R.J. Beyers, R.C. Cattley, I. Ivanović-Burmazović, D.D. Schwartz, C.R. Goldsmith, *Inorg. Chem*., **56** (2017) 2812-2826.
9. S.L. O'Neal, W. Zheng, *Curr. Environ. Health Rep*., **2** (2015) 315-328.
10. E.M. Gale, S. Mukherjee, C. Liu, G.S. Loving, P. Caravan, *Inorg. Chem*., **53** (2014) 10748-10761.
11. E.M. Gale, I.P. Atanasova, F. Blasi, I. Ay, P. Caravan, *J. Am. Chem. Soc*., **137** (2015) 15548-15557.
12. G.S. Loving, S. Mukherjee, P. Caravan, *J. Am. Chem. Soc*., **135** (2013) 4620-4623.
13. F. L'Eplattenier, I. Murase, A.E. Martell, *J. Am. Chem. Soc*., **89** (1967) 837-843.
14. R.J. Motekaitis, A.E. Martell, M.J. Welch, *Inorg. Chem.*, **29** (1990) 1463-1467.
15. I. Kenkel, A. Franke, M. Dürr, A. Zahl, C. Dücker-Benfer, J. Langer, M. Filipovic, R., M.

Yu, R. Puchta, S.R. Fiedler, M.P. Shores, C.R. Goldsmith, I. Ivanović-Burmazović, *J. Am. Chem. Soc.*, **139** (2017) 1472-1484.

16. Q. Zhang, J.D. Gorden, R.J. Beyers, C.R. Goldsmith, Inorg. Chem., 50 (2011) 9365-9373.
17. M.A. Bernstein, K.F. King, X.J. Zhou, Handbook of MRI Pulse Sequences, Elsevier Academic Press, Amsterdam, 2004.
18. E.M. Haacke, R.W. Brown, M.R. Thompson, R. Venkatesan, Magnetic Resonance Imaging: Physical Principles and Sequence Design, John Wiley & Sons, New York, NY, 1999.
19. J.A. Nelder, R. Mead, *Comput. J.*, **7** (1965) 308-313.
20. J. Yoon, J.-S. Ryu, *Bioorg. Med. Chem. Lett.*, **20** (2010) 3930-3935.
21. M.B. Ward, A. Scheitler, M. Yu, L. Senft, A.S. Zillmann, J.D. Gorden, D.D. Schwartz, I. Ivanović-Burmazović, C.R. Goldsmith, *Nature Chem.*, **10** (2018) 1207-1212.
22. A. Franke, A. Scheitler, J.L. Moore, S. Sader, S. Ison, I. Ivanović-Burmazović, C.R. Goldsmith, in, 2019.
23. C.R. Goldsmith, A.P. Cole, T.D.P. Stack, *J. Am. Chem. Soc.*, **127** (2005) 9904-9912.
24. T.J. Hubin, J.M. McCormick, N.W. Alcock, D.H. Busch, *Inorg. Chem.*, **40** (2001) 435-444.
25. J.T. Henthorn, S. Lin, T. Agapie, *J. Am. Chem. Soc.*, **137** (2015) 1458-1464.
26. I.R. Corn, P.D. Astudillo-Sánchez, M.J. Zdilla, P.E. Fanwick, M.J. Shaw, J.T. Miller, D.H. Evans, M.M. Abu-Omar, *Inorg. Chem.*, **52** (2013) 5457-5463.
27. M.R. Haneline, A.F. Heyduk, *J. Am. Chem. Soc.*, **128** (2006) 8410-8411.
28. T. Hirao, *Coord. Chem. Rev.*, **226** (2002) 81-91.
29. T.W. Myers, L.A. Berben, *Inorg. Chem.*, **51** (2012) 1480-1488.
30. D.L.J. Broere, R. Plessius, J.I. van der Vlugt, *Chem. Soc. Rev.*, **44** (2015) 6886-6915.
31. O.R. Luca, R.H. Crabtree, *Chem. Soc. Rev.*, **42** (2013) 1440-1459.

32. F.A. Cotton, G. Wilkinson, Advanced Inorganic Chemistry, 5 ed., John Wiley & Sons, New York, 1988.

33. P. Caravan, J.J. Ellison, T.J. McMurry, R.B. Lauffer, *Chem. Rev*., **99** (1999) 2293-2352.

34. A. Cusanelli, U. Frey, D.T. Richens, A.E. Merbach, *J. Am. Chem. Soc*., **118** (1996) 5265-5271.

35. D. Lieb, F.C. Friedel, M. Yawer, A. Zahl, M.M. Khusniyarov, F.W. Heinemann, I. Ivanović-Burmazović, Inorg. *Chem.*, **52** (2013) 222-236.

36. F.C. Friedel, D. Lieb, I. Ivanović-Burmazović, *J. Inorg. Biochem*., **109** (2012) 26-32.